

Analysis of optical properties of the baffles for a laser-based dust logger to be deployed in the IceCube Upgrade

Bachelor's Thesis in Physics

Presented by
Dean Eric Fleischmann
02.08.2024

Erlangen Centre for Astroparticle Physics
Friedrich-Alexander-Universität Erlangen-Nürnberg



Supervisor: Prof. Dr. Claudio Kopper

Abstract

The IceCube neutrino observatory[1] is a neutrino detector located at the geographic South Pole instrumenting 1 km^3 . Neutrinos are indirectly detected via secondary particles producing Cherenkov radiation, which traverses the ice and are detected by optical sensors.

The optical properties of the instrumented ice needs to be well understood to properly reconstruct the neutrino events [2]. For this the stratigraphy measurements of the ice are done. One method for measuring the stratigraphy of ice is dust logging. This works by measuring the scattering length of the ice with a laser system while deployment. For the IceCube Upgrade, a new dust logging device, called LOMlogger will be used. To ensure the detected light is only the light scattered in ice and not the light passing through the borehole directly to the detector. The path through the borehole is blocked via a baffle.

In this thesis the optical properties of the baffle will be investigated in an experiment as well as the optimal placement of the baffle via simulation of the borehole. The optimal placement of the baffle is found out to be close to the POCAM. It was additionally found that the borehole diameter has a larger impact on the effectiveness of the baffle.

Contents

1	Introduction	1
1.1	Neutrino astronomy	1
1.2	The IceCube detector	2
1.3	IceCube Upgrade and Gen2	3
1.4	Ice optical properties	5
1.5	Stratigraphy measurement	6
1.5.1	Dust logger	6
1.5.2	LOMlogger	7
1.5.3	The baffle	9
2	Experiment	11
2.1	Setup	11
2.2	Measurement	12
2.3	Simulation of the experimental setup	15
2.4	Results	18
3	Simulation	19
3.1	Scattering in ice simulation	19
3.2	Simulation of the borehole	20
3.2.1	Setup	20
3.2.2	Different angle between source and detector	21
3.2.3	Scattering length	23
3.2.4	Only backside of detector	25
3.2.5	Changing hole diameter and baffle position	26
3.2.6	Position where the baffle gets hit	27
4	Conclusion	29
A	Test of the experimental results	34
B	Errors on the experimental results	35
	Bibliography	38

1 Introduction

As introduction and general context to my thesis an overview about the different topics related to my thesis is given. Starting with a general introduction to neutrino astronomy and the IceCube detector. The IceCube detector instruments a cubic kilometer of ice. This ice needs to be well understood, therefore introductions to the ice optical properties and stratigraphy are given, in particular dust logging. The new version of the dust logger, the LOMlogger is also introduced.

1.1 Neutrino astronomy

Neutrinos are neutral elementary particles, they were first postulated by Wolfgang Pauli in 1930, to preserve the conservation of energy during the β -decay [3]. In the standard model there are three different flavors of neutrinos, one for each charged lepton. The standard model assumes that neutrinos do not have a mass, this cannot be true given our current understanding of neutrinos. The main reason being neutrino oscillation. Neutrino oscillation is the mechanism by which neutrinos change their flavors while propagating through space. This leads to neutrinos needing to have mass. It was first proposed by Bruno Pontecorvo in 1957 [4] and experimentally observed in the 70s by Ray Davis in the Brookhaven Solar Neutrino experiment [5], and by many others after him.

Neutrinos only interact via the weak force. This makes them incredibly evasive and hard to detect. The only way to detect neutrinos is by them interacting and producing a charged secondary particle, like an electron, muon, or tau. These secondaries can then be detected e.g. via Cherenkov radiation. Cherenkov radiation is emitted when a high-energy charged particle enters a dielectric medium with a velocity greater than the speed of light inside that medium. The Cherenkov light is emitted in a cone, similar to a sonic boom, as seen in Figure 1.

The pattern of the Cherenkov light provides information about the neutrino. Electron

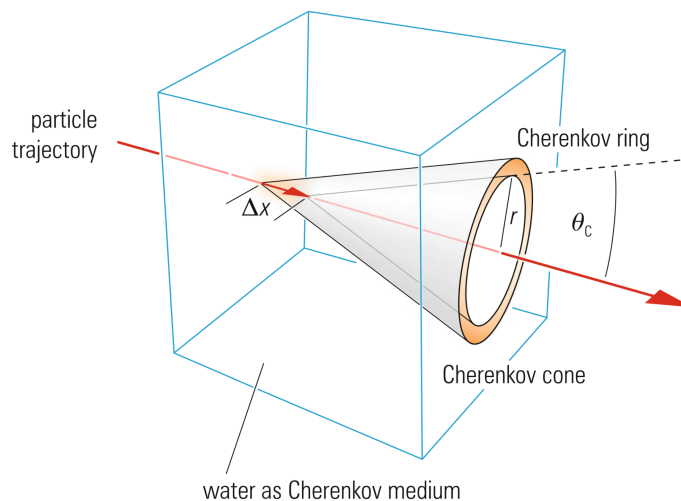


Figure 1: A sketch of the Cherenkov cone for an incoming particle inside a water Cherenkov detector. The opening angle of the cone depends on the medium [6].

neutrinos produce high-energetic electrons, which produce electromagnetic cascades of short range which result in more diffusive Cherenkov cones. These events are called cascade-like. Muon neutrinos produce high-energetic muons, these have a well-defined range and produce sharper Cherenkov cones. These events are called track-like [7].

Since neutrinos have a small interaction cross-section the volume of the dielectric

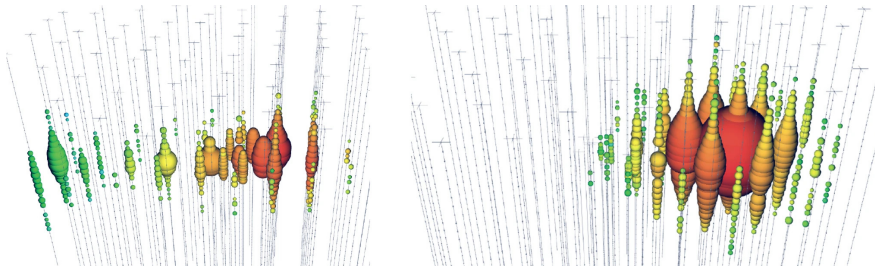


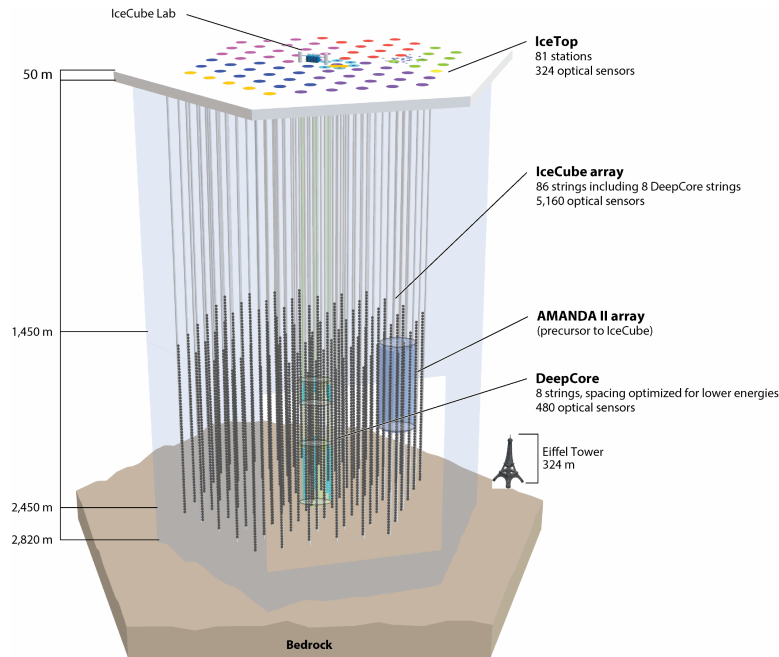
Figure 2: This image shows two example events of IceCube. Left an example for a track-like event in IceCube produced by a muon neutrino and right an example for a cascade-like event produced by an electron or tau neutrino [8]. The color corresponds to the time when the optical module was activated and the size of the sphere to the deposited energy at the optical module.

medium to obtain a decent event rate must be on the magnitude of a cubic kilometer. Building such a large dielectric medium is currently not possible, therefore nature itself needs to be used. There are two transparent media used for neutrino detectors, water and ice. Both can be found in large volumes and with a high homogeneity. For water, there are currently multiple neutrino detectors in operation under construction, like KM3NeT[9] and P-One[10]. One currently existing neutrino detector in ice is IceCube.

1.2 The IceCube detector

IceCube was the first neutrino detector to reach one cubic kilometer of instrumented detector volume [3]. IceCube is located in Antarctica near the Amundsen-Scott South Pole Station and consists of 5160 optical sensors, called digital Optical Modules (DOMs). These modules were deployed at a depth between 1450 m and 2450 m on cables with 60 modules per cable at a total of 86 locations, a drawing of this can be seen in Figure 3. To reach these depths a hot water drill was used to drill boreholes into the ice. These boreholes were 60 cm wide and had a depth of 2500 m. The melted ice resulting from the drilling process stayed in the borehole. This is the reason why the borehole diameter was larger than the DOM diameter with only 45 cm. To account for refreezing of the borehole during deployment. The DOMs attached to the strings are then deployed into the borehole and sink to their desired positions [11].

The observable event energy range of IceCube is between a few GeV and multiple PeV [12]. This means IceCube observes atmospheric and astrophysical neutrinos. Atmospheric neutrinos are produced in the earth's atmosphere by cosmic rays. Astrophysical neutrinos are produced in high-energy events like supernovae or inside the jets of black holes [7]. Neutrinos produced in these events have the advantage over other cosmic rays produced, in that they are chargeless and therefore not affected by magnetic fields. Their small interaction cross section is here an advantage in that they are not absorbed by the source itself or the matter they traverse until reaching us. Thanks to this it is possible




 Gaissner T, Halzen F. 2014.
 Annu. Rev. Nucl. Part. Sci. 64:101–23

Figure 3: Artist’s drawing of IceCube at the National Science Foundation’s Amundsen–Scott South Pole Station. The former AMANDA detector is shown in blue and the DeepCore subarray in green [13].

to reconstruct the point of origin, just from the arrival direction of the neutrino. Since the neutrino is not detected, but only a secondary particle, the arrival direction of the neutrino has to be reconstructed from the arrival direction of the secondary particle. This leads to the angular resolution depending on the reconstruction of the event and the type of the event. The IceCube events can be sorted into two groups, cascade-like events and track-like events.

To distinguish the atmospheric from the astrophysical neutrinos, one must look at the energy and direction of the detected neutrino, an excess of neutrinos in a given region of the sky or an excess at high energies would lead to the assumption that these neutrinos are extraterrestrial. The first evidence for a constant astrophysical neutrino flux was given by [14]. Meanwhile, it is accepted that IceCube sees an astrophysical neutrino flux [15]. And that there is an astrophysical flux originating from the galactic plane. This flux originates from high energetic particles interacting with the dust of the galactic plane [16]. IceCube was able to assign individual neutrino events to the blazar TXS 0506+056. These were coincident in direction and time with gamma-ray flares, suggesting blazars as neutrino sources [17].

1.3 IceCube Upgrade and Gen2

In order to advance neutrino astronomy further, bigger and better neutrino detectors have to be built. To build upon IceCube’s success there are currently two upgrade phases in planning and under construction. The first is the IceCube Upgrade, the

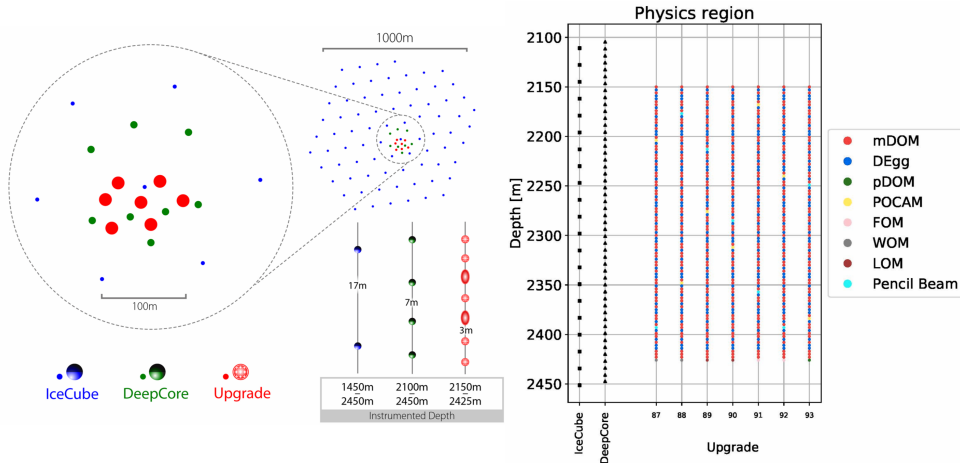


Figure 4: The upgraded array geometry. On the left side the horizontal cross-section of the Upgrade, in red marked the Upgrade strings. On the right side the occupation of the seven detector strings used in the Upgrade compared to the IceCube and DeepCore strings [18].

deployment of the Upgrade is planned for the 2025/2026 Antarctic summer [18, 19]. The Upgrade will consist of seven detector strings with approximately 700 optical sensors. It will instrument the bottom center of the existing IceCube detector at a depth between 2150 m and 2425 m [18]. The strings are more densely populated than the original IceCube strings. The denser grid of optical modules leads to a decrease in the energy threshold to a few GeV and with that to more accurate measurements of atmospheric neutrinos. The gained sensibility leads to IceCube improving its ability to perform atmospheric neutrino oscillation measurements with high sensitivity [20].

The Upgrade uses multiple different types of optical modules, the two most common ones are the mDOM (multi-PMT digital Optical Module) and the D-Egg (Dual optical sensors in an Ellipsoid Glass for Gen2). The placement along the string of the different optical modules can be seen in Figure 4. The mDOM consists of 24 PMTs (Photomultiplier Tubes) orientated along all directions of the sphere. This leads to a nearly isotropic sensitivity. The D-Egg consists of two PMTs one orientated upwards and one downwards. The up-facing PMT will enable better background muon rejection [20]. The new optical sensors are expected to significantly increase the angular resolution of the array.

There are new devices and sensors added inside the spheres of the optical modules, these will provide new abilities to calibrate the existing detectors. There are also new stand-alone devices attached to the strings, like the POCAM (precision optical calibration module) [18]. The POCAM is a multipurpose calibration device consisting of four LEDs as light sources, and a Silicon-Photomultiplier and a photodiode as sensors. The LED wavelengths range between 300 nm and 600 nm. The LEDs can achieve pulses with FWHM of 1-8 ns. On top of the LEDs is an integrating sphere which leads to an isotropic emission of the POCAM. The sensors can measure the in-situ intensity characteristics and the pulse time onset with a precision of a few percent. It aims to better understand and reduce the systematical experimental uncertainties. In particular

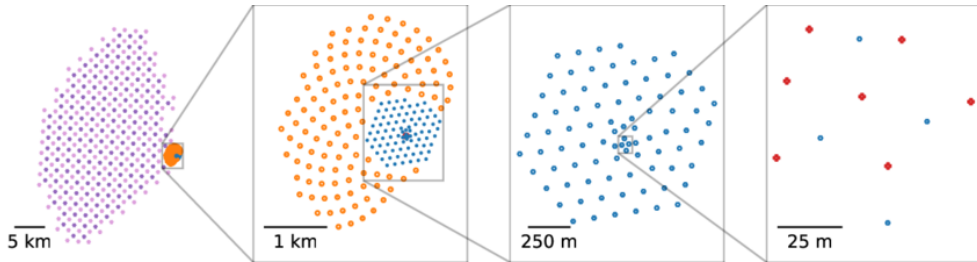


Figure 5: The Gen2 array geometry compared to the Upgrade and IceCube and the radio array. Starting on the left site with the radio array, then Gen2, IceCube and the Upgrade [23].

the uncertainties of the optical sensors [21]. The better calibrations of the detector are expected to enhance the angular resolution of current IceCube data for high-energy neutrinos to better than 0.3° for track-like events and better than 5° for cascade-like events [12]. The IceCube Upgrade will improve the performance of the total detector array, as well as pave the way for the future IceCube-Gen2.

Gen2 is the planned second phase of the IceCube array extension, but is currently on hold. It would increase the detector volume to 8 km^3 with 120 additional strings, as seen in Figure 5. Each string would consist of 80 equally spaced optical modules over an instrumented depth of 1.25 km. Similar optical modules to the IceCube Upgrade would be used, so called LOMs (long Optical Module). These are elongated versions of the mDOM with 16 to 18 PMTs, the elongated form empowers the LOM to be deployed in boreholes with smaller radius [22]. This will lead to an overall improvement in event rate by a factor between 4 and 10, depending on the event type, and an increase of the angular resolution by approximately a factor of three. In Gen2 an ultra-high-energy radio array would be implemented stretching over vastly larger area than the rest of the detector array as seen in Figure 5. This would expand the obtainable energy range for astrophysical neutrinos up to 100 EeV [12].

1.4 Ice optical properties

Ice as a detector medium comes with a few challenges. The Cherenkov light produced by the neutrino interaction has to propagate through the ice until it reaches the detector. While propagating it interacts with the impurities inside the ice, which leads to scattering and absorption of the light. These effects must be accounted for when reconstructing the neutrino event [24].

Important parameters for the optical properties of the ice are the geometric scattering length λ_b , which is the average distance between successive scatterings. The angle at which the light is scattered θ . The probability for the light to scattering in a given angle θ can often be described by a probability distribution $P(\theta)$. The absorption length λ_a is the distance at which $1/e$ photons have not been absorbed. The absorption lengths in IceCube are a few hundred meters [2].

The leading cause of scattering in the South Pole ice are air bubbles, which are trapped during snowfall and freeze into the ice [25]. At a depth of around 1300 m the pressure is high enough that the air bubbles disappear. At deeper depths, the scattering is

mainly due to dust particles trapped during snowfall [26]. Scattering on small particles is described by Mie scattering.

For the simulation in this thesis, an approximation of Mie scattering is used. This approximation is the Henyey-Greenstein phase function [27]. It assumes that the scattering is forward peaked. This is the case for ice which has strong forward scattering [2]. The Henyey-Greenstein phase function describes the probability distribution of each scattering angle $P_{HG}(\cos(\theta))$.

$$P_{HG}(\cos(\theta)) = \frac{1 - g^2}{2(1 + g^2 - 2g \cos(\theta))^{\frac{3}{2}}} \quad (1)$$

θ is here the scattering angle and g is the mean of the cosine of the scattering angle, $g = \langle \cos(\theta) \rangle$ [27]. Ice has strong forward scattering and with that a g of approximately 0.95. λ_b and g are degenerate in the far field and therefore often the effective scattering length λ_{eff} is used [27, 28]. It is the distance at which the photon direction becomes effectively randomized. [24, 2].

$$\lambda_{eff} = \frac{\lambda_b}{1 - g} \quad (2)$$

The cleanest ice in IceCube has an effective scattering length of 84 m, and the dirtiest ice has an effective scattering length of around 20 m. The big discrepancy originates from a varying amount of dust in the atmosphere during the ice formation [2].

1.5 Stratigraphy measurement

Stratigraphy investigates the depth dependence of different sediments. This depth dependence originates from different environmental conditions during the time the sediment formed. In IceCube the stratigraphy is measured to examine the different ice depths and their optical properties. Especially the effective scattering length as well as the absorption length of the ice depends on the amount of impurities inside it. The amount of impurities depends mainly on the amount of dust inside the atmosphere during ice formation. Big events like volcanic eruptions can also be seen in the different interaction lengths of the ice. With these events, the age of the ice can be determined [26].

1.5.1 Dust logger

The stratigraphy in IceCube was originally measured with a laser system, called the dust logger [26]. The dust logger was deployed into eight of the 86 boreholes in IceCube. The first two dust loggers were permanently attached to the detector strings and therefore not retrieved. In the other six boreholes the dust logger was deployed prior to the string and retrieved after the measurement.

The dust logger consists of a light source shining light into the ice perpendicular to the borehole. The light source is a diode laser with a wavelength of 404 nm and a span of 60° of the horizon. The wavelength is in the range of expected Cherenkov radiation and where the ice has its lowest absorption [29]. The 60° span averages over a larger portion of the same ice depth. The light is scattered back inside the ice onto the detector of the dust logger, as seen in Figure 6. The detector is a downward-facing photon-counting detector. Two nylon ring brushes are placed between the source and the detector, these

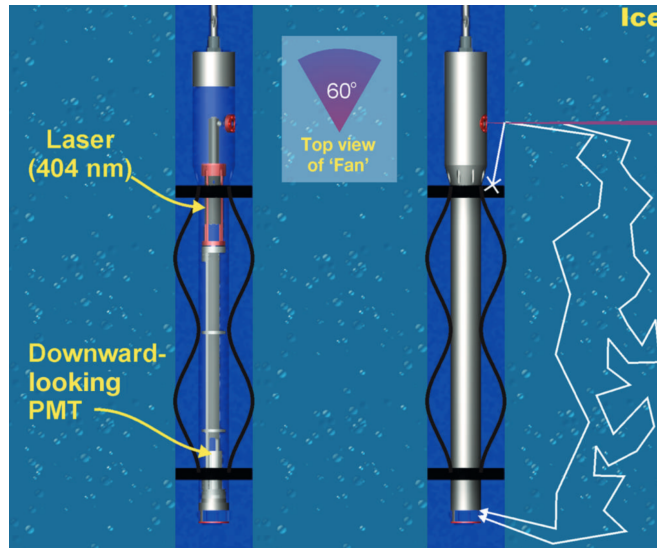


Figure 6: Laser dust logger deployed in IceCube [26].

are supposed to block the light scattered and reflected inside the borehole, so that only the light scattered in the ice is detected.

The depth position of the dust logger is measured by pressure sensors, resulting in an offset of 1-2 m. The depth was also measured by the length of cable that was deployed leading to a high sensitivity. Light intensity measurements were taken every 2-3 mm. The logger data is aligned with prior ice core measurements to obtain common distinct features. The aligning works by finding equal distinct features in the data and correcting for the mismatch in depth [26].

The dust logger measurements resulted in high-resolution stratigraphy data of the South Pole ice in good agreement with ice core measurements. This allows more accurate event reconstruction in IceCube. The measurements also perform as reference points to model the ice layer tilt. Ice layers are ice sheets with roughly the same optical properties over the full array. These ice layers are not at the same height over the full array. This leads to a tilt of the layers compared to the horizon. The reason for this tilt is the ice flow and the bedrock topology, which leads to the undulation [30]. The data taken by the dust logger showed an increasing tilt of the ice sheets close to bedrock which confirms the bedrock as origin of the tilt. The data showed an undulation of the layers of around 10%. 10% undulation mean here over a given distance a change of elevation of 10% of the distance (0.1 km elevation change over 1 km distance) [26]. If the undulation is not known this results to problems for the reconstruction because one would expect different ice layers at different depths. This is particularly important for IceCube Gen2 because Gen2 instruments a way larger detector volume. This results into undulation having a larger effect in Gen2. Showing that dust logging will be particularly important for Gen2.

1.5.2 LOMlogger

The LOMlogger is a new version of the laser stratigraphy system used in the original IceCube deployment (the dust logger). It will be first used in the IceCube Upgrade.

Similarly to the not retrievable dust loggers, the LOMlogger will be co-deployed with the detector strings and not retrieved. The design of the LOMlogger is similar to the dust logger but with new hardware, and it is not deployed in one casing, but each part is an individual module, as seen in Figure 7. The LOMlogger has not its own PMT as a



Figure 7: 3D-model of the LOMlogger. The LOM at the top, the baffle in between, and the POCAM at the bottom. The distance between LOM and POCAM is 2 m. The LOM is used as the detector of the LOMlogger and the POCAM as the source [19].

detector. But rather uses one optical module of the detector string as detector. This module will also be used after the stratigraphy measurement in contrary to the PMT of the dust logger. The optical module used is the LOM. The LOM is an optical module designed for IceCube Gen2 it consists of 18 or 16 PMTs and will be first tested in the Upgrade. It is elongated compared to the mDOM to fit in boreholes with a smaller diameter, reducing fuel use of the drill and drilling time. The LOM has an almost homogeneous angular coverage [31].

The POCAM[21] is used as a light source. The POCAM can produce isotropic, nanosecond light pulses and will be used for optical calibrations in the IceCube Upgrade. For the LOMlogging a modified version of the POCAM is used. This version uses a laser diode with a wavelength of 405 nm as the light source. This laser diode beam is then collimated and fanned out by 60° similar to the dust logger [32]. The POCAM is placed in a steel harness and secured to LOM and baffle, as seen in Figure 7.

The LOMlogger deployment in the Upgrade will obtain stratigraphy data in deep ice

below IceCube and is a first test for the planned deployment in IceCube Gen2 [33]. The LOMlogger is planned to get stratigraphy data over the full Gen2 array during the Gen2 deployment. This will allow a model of the tilt of the ice layers over the full array and with that a decrease in event energy uncertainty. This is particularly important due to the large horizontal string spacing in Gen2 [33].

1.5.3 The baffle

The baffle that was proposed for the LOMlogging is a ring brush with a diameter of 50 cm. The current baffle that is used for this thesis is a ring brush of the type SV8 from the company bmt [34] with the desired outer diameter of 50 cm and an inner diameter of 15 cm. It consists of around 2000 bristles made from PBT (Polybutylenterephthalat) with each bristle having a diameter of 0.8 mm, a picture of the baffle is shown in Figure 8a.

For the simulations in this Thesis, the baffle has to be recreated in a 3D-modeling

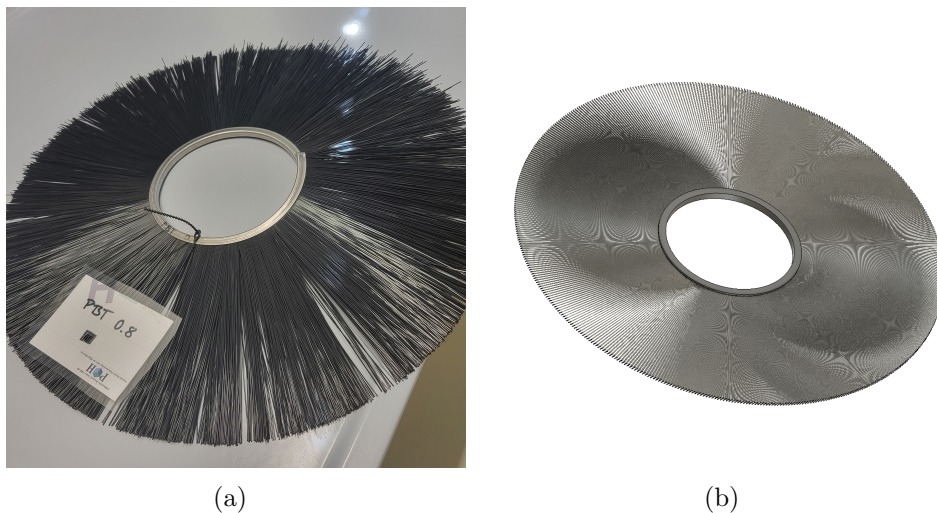


Figure 8: a) Shows an image of the baffle used in the experiment. b) Shows the designed baffle in fusion.

software, for this Autodesk Fusion [35] was used. The number of bristles for a 10° segment of the baffle were counted. From this, the number of bristles was approximated to be 2348. Visually the bristles were placed in four or five rows, I chose five to be more fitting. This leads to 468 bristles per row. Each row of bristles was placed slightly off axis, to fan the bristles out more realistically. The other parameters of the baffle were copied from the existing baffle. The final 3D model can be seen in Figure 8b, this model will be used for the coming simulations.

The baffle needs to be held in place between the LOM and the POCAM. This is done by clipping the baffle between the steel wire structures of the LOM and the POCAM, as seen in Figure 7. These steel wire structures are normally used to combine two optical modules and form in total the detector string. To secure these steel wires to the baffle a holding structure is designed. The holding structure consists of two cylindrical parts with the baffle in between, they are held together by a steel eye bolt and eye nut, as seen in Figure 9a. The carabiner of the steel wire structure is connected to the eyes of

the eye bolt, as seen in Figure 7.

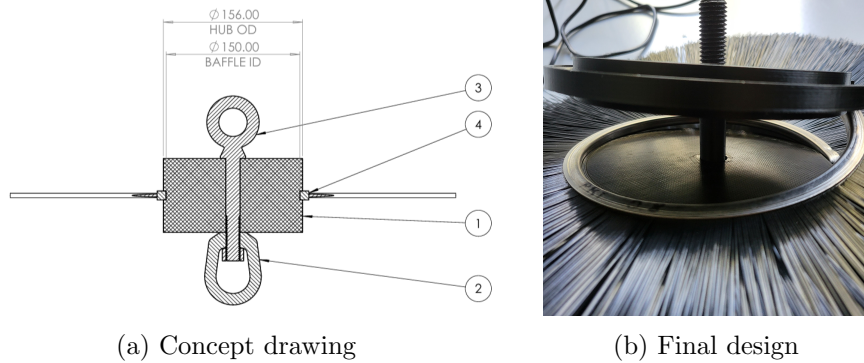


Figure 9: a) The concept drawing of the baffle holding structure. 1) The holding structure, in the final design it is made out of two symmetrical parts. 2) The steel eye nut and 3) the steel eye bolt. 4) The baffle. b) The final design seen in the image is not screwed together, missing the eye nut. The part seen above is symmetrical and placed also under the baffle. The design is cascadable, allowing to easily stack multiple baffles on top of each other.

2 Experiment

The experiment aims to obtain quantitative values for the absorption of the baffle. For this purpose, an experimental setup was designed, and the absorption of the baffle was tested at three radial- and six angular positions. With this, the absorption of the baffle was mapped. The experimental setup was recreated in a simulation in Zemax Opticstudio [36]. Different designs of the baffle were created in Fusion Autodesk [35], implemented in the simulation, and compared to the measurement results. With this, the most accurate representation of the experimentally used baffle was adapted for the coming simulations.

2.1 Setup

In this chapter, the setup of the experiment is discussed in detail. The usage of each component is explained. And all components are listed with additional details.

To mimic the absorption of the baffle in the borehole as closely as possible, the baffle will be submerged in water for the full experiment. For this purpose, the baffle is placed inside the bucket filled with water. To mimic the borehole, a tube equal to the diameter of the baffle, is placed around the baffle. In a wooden plank, five holes of a diameter of 2.2 cm are drilled with a distance between each hole of 13 cm. In each hole one flasher is placed, meaning 5 flashers are used for the experiment. The plank is placed on top of the bucket and the center flasher is aligned with the center of the baffle. The photodiode will be placed at different radial positions relative to the center of the baffle and on the axis parallel to the wooden plank, a sketch of the setup can be seen in Figure 10a.

The used components are:

Flasher As the light source for the experiment, mDOM calibration system flashers [37] are used. These contain a RLT405-600MGE LED from Roithner [38] with a wavelength of 405 nm, equal to that of the LOMlogger. The uncollimated beam has an FWHM (full width at half maximum) in intensity of 15° . The flasher always emits pulses, the frequency and intensity of these pulses can be controlled via a python program. The flashers are placed in a 3D-printed casing and covered with epoxy. This makes them waterproof.

Photodiode The detector is a S2281-01 Si photodiode from Hamamatsu [39]. The photodiode is mounted to a preamplifier circuit, this is a similar setup as it was used in [40, 37]. The integration time of the photodiode is 4 s, this is considered in the readout code. To make the photodiode waterproof it is placed in a 3D-printed casing and covered with epoxy.

Baffle The baffle as described in section 1.5.3 is used. The baffle is secured inside the baffle holding structure and placed on top of the baffle stand.

Tube The tube has a diameter of 50 cm and a height of 17 cm and a neglectable thickness, it is made out of aluminum. The tube is used to mimic the borehole.

90 L bucket A nearly cylindrical 90 L bucket with a radius of 33 cm and a height of 34.5 cm is used as the water tank and is filled with water up to a height of 22 cm. The baffle, the photodiode, and the tube are placed inside this bucket.

Baffle stand The baffle stand is a 3D-printed tube with a height of 12.5 cm, a radius of 4 cm and a thickness of 3 mm. The baffle stand is used to keep the baffle at a constant height for all measurements.

Blanket A black blanket is used to cover the setup, this is done to block the photodiode from ambient light.

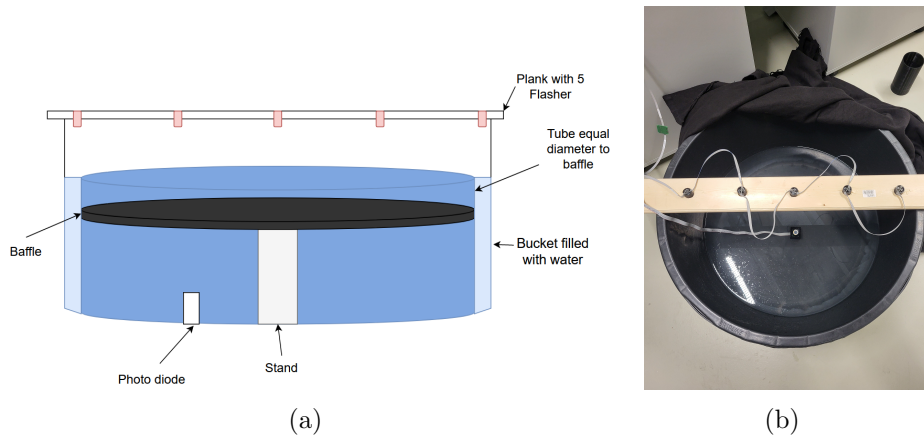


Figure 10: a) The image shows a sketch of the experimental setup. b) Shows a picture of the experimental setup without the baffle, the photodiode will be placed further left for the measurement.

2.2 Measurement

The objective of this measurement is to deduce any angular or radial dependencies of the transmittance for the baffle. For this the transmittance of the baffle is measured at 18 different angular and radial positions. To achieve consistent results the setup in section 3.2.1 is used. To measure the transmittance for the different angular position the baffle is rotated and for the radial positions the photodiode is moved. From knowing the position of the photodiode and the closest flasher we can calculate at which position we measured the transmittance. The reason for this is that the flasher closest to the photodiode is the main source of the intensity on the photodiode (see Appendix A). This means the light detected on the photodiode has passed through the part of the baffle on the direct line between the flasher and the photodiode. If the intensity of the different placements of the photodiode is measured with and without the baffle, the light blocked from that part of the baffle can be calculated.

An example measurement is done, as a first test and to show the process of a measurement. The photodiode is placed at a not-controlled position under the wooden plank and the setup is covered with the blanket. The photodiode measures for roughly 75 s, during the measurement the flashers are turned on for 30 s. The same measurement is done with the baffle. Both measurements are shown in Figure 11, in both measurements the time when the flashers are turned on is visible, after around 25 s. This shows that the flasher system and the photodiode work. The error on the measured values is the standard deviation of the mean, calculated for on and off phases individually and with and without the baffle. The mean for the photodiode voltage without the baffle is

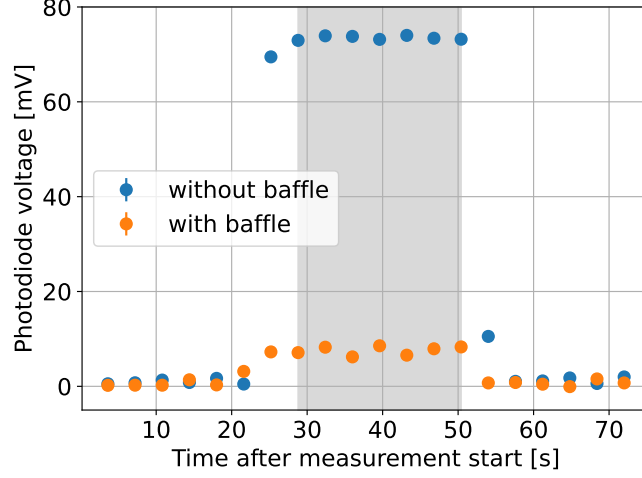


Figure 11: The detected photodiode voltage is plotted over the time after the measurement started, for the measurement with and without the baffle. The data points with a gray background were taken for the mean.

73.50 ± 0.38 mV and with the baffle 7.56 ± 0.85 mV. To calculate the light transmitted through the baffle ε the quotient of both means is taken:

$$\varepsilon = \frac{I_{wb}}{I_{wob}} \pm \frac{1}{I_{wob}} \sqrt{\sigma_{wb}^2 + \left(\frac{I_{wb} \cdot \sigma_{wob}}{I_{wob}} \right)^2} \quad (3)$$

I_{wb} and I_{wob} are the detected intensities with and without the baffle respectively, and σ_{wb} , σ_{wob} their errors. The error on ε is calculated via Gaussian error propagation from the error of the two intensities. With this, the light that is transmitted through the baffle in the verification measurement is $10.3\% \pm 1.1\%$ of the light without the baffle. This shows that the baffle is blocking light and the setup is precise enough for the upcoming measurement.

The measurement is done for six angular and three radial positions. To precisely know the angular position of the baffle, the baffle holding structure was marked every 60° . To measure the six different angular positions the baffle is each time rotated by an additional 60° . To measure the radial dependence of the baffle the photodiode is placed at three different radial positions, the center of the photodiode marks the radial position. The three different radial positions are at a radius of 10 cm, 16 cm, and 22 cm. The measurement starts at a radius of 10 cm and not 0 cm because the bristles only begin at a radius of 8 cm. The light at any position smaller than the 8 cm would not pass through the bristles but through the baffle holding structure which is fully absorbing. For this measurement, every flasher is turned on with its maximum intensity and a frequency of 1000 Hz. The frequency of the flasher is magnitudes higher than the readout frequency of the photodiode, meaning the intensity detected on the photodiode is the intensity per pulse summed over the readout time.

For each position of the photodiode 30 on-off cycles of the photodiode are taken and averaged over. In Figure 12 the transmittance of the baffle for all 18 measurements is shown. It is apparent that the light transmitted through the baffle rises consistently with larger radii, this is because the area that the bristles of the baffle block stays

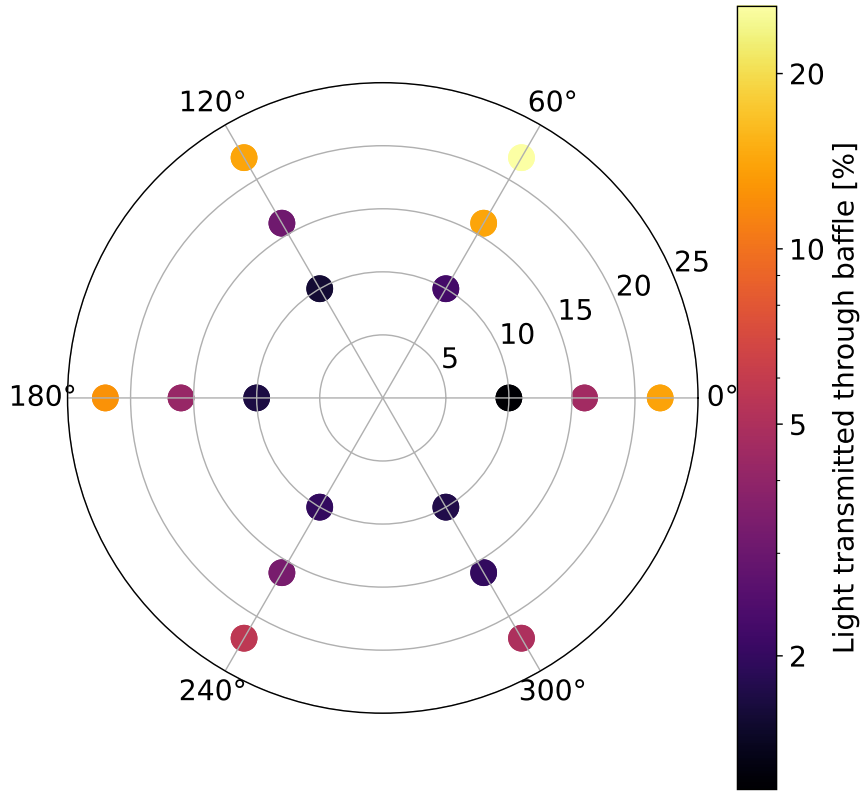


Figure 12: The crosses show the 18 different measured positions of the photodiode under the baffle in polar coordinates. The color shows the amount of light transmitted through the baffle in percent.

constant for a ring with changing radius and constant thickness. This means the area that the bristles block at a larger radius is smaller relative to the area without bristles. This leads to an increase in transmittance for larger radii.

It is apparent in the plot that there are large fluctuations in transmittance for the same radii but changing angles. One big outlier is the measured position of 60° with the largest radius, which has by far the highest transmittance. An explanation for this might be the ability of the bristles to clump into bunches, leaving larger gaps at some angles, as seen in Figure 13. These lead to a higher-than-average transmittance.

The error on the transmittance is calculated with Equation 3. The error of the individual intensities is the standard deviation on the mean of each measurement. The errors on the transmittance are generally small and displayed in Appendix B. The errors are small enough to reasonably interpret the results.

The position of the flashers was not optimal for the experiment. A more optimal use of the flashers would have been to only use one flasher placed directly above the photodiode. This would assure that the light reaching the photodiode would have passed the baffle directly above it, and did not scatter from a different source. After realizing this the measurement was not repeated due to time constraints. The values of the experiment are still representative as the light reaching the photodiode is still originating from the closest flasher and the actual position of the light passing the baffle can be calculated.

This is shown in the simulation in Appendix A.



Figure 13: The image highlights a part of the baffle, where the bunching of the bristles is pronounced.

2.3 Simulation of the experimental setup

The simulation is designed to represent the experiment in its most essential way. The objective of the simulation is to find a matching baffle model to the experimentally used baffle. The simulation is done with Zemax Opticstudio [36].

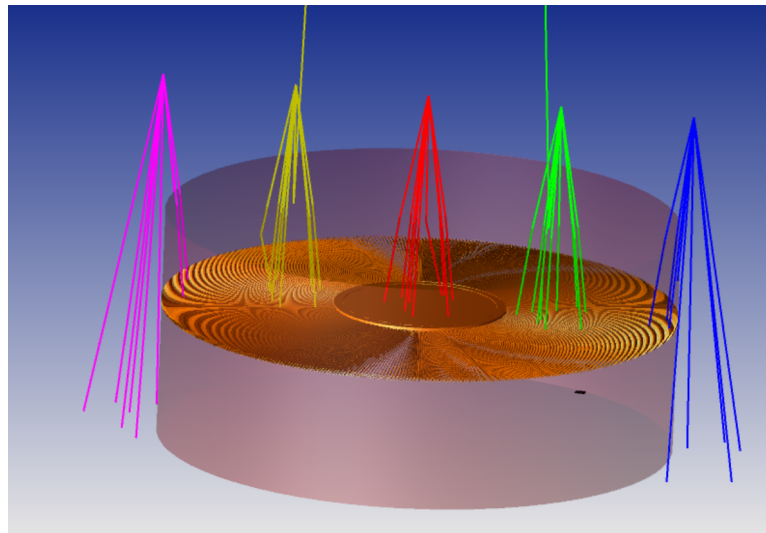


Figure 14: The image shows the setup of the simulation, with the original baffle model.

Flasher The five flashers are recreated with five point sources. Each point source has a cone of 15° and a distance to the next flasher of 13 cm. The center flasher is aligned with the center of the simulation.

Tube The tube is simulated as a water cylinder with a diameter of 50 cm and a height of 22 cm, equal to the height of the water in the experiment. The sides of the

cylinder as well as the bottom are implemented to be fully absorbing, this is a good enough approximation to the aluminum of the tube. The bucket is not simulated due to there being no need to contain the water in the simulation and the bucket having no other effect on the measurement.

Photodiode The photodiode is approximated with a square detector of 1 cm^2 at a height of 6 cm, this is equal to the height of the photodiode. The radial positions of this detector are measured the same way as in the experiment.

Baffle The baffle was modeled in Fusion as described in section 1.5.3. To find the best approximation of the baffle, four different baffle models are used. The original baffle model described in section 1.5.3 has five rows of bristles with each having 468 bristles. The next three baffle models each have half a row fewer bristles. The bristles with baffle models with half rows are distributed, so that these are radial symmetric. For each simulation, one baffle model is placed inside the cylinder at a height of 13 cm, without the baffle stand because this is not needed in the simulation and has no effect on the results.

The light transmitting through the baffle models is simulated at five different radial positions, the angle is not changing because all baffle models are radially symmetrical. One simulation without a baffle is done for all radial positions, with this, the transmittance of the baffle models can be calculated (see Equation 3). For comparison, the mean of each radial position for all angles in the experiment is calculated and plotted in Figure 15b. The radial position is that of the photodiode and not the exact point at which the light passes the baffle, as discussed in Appendix A. This does not matter for the fit because we only compare the values, and this offset is the same for every measurement.

It is evident in Figure 15a that the standard deviation and the mean without the

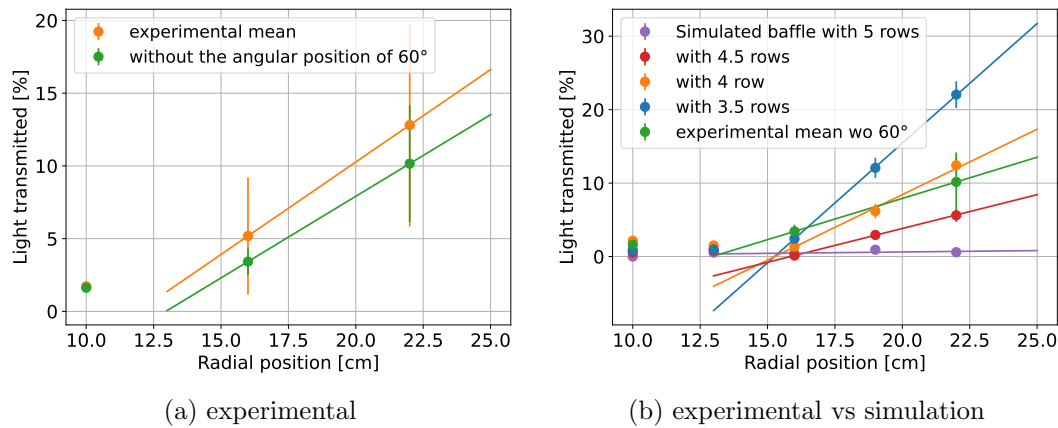


Figure 15: a) Shows the calculated mean light transmittance with the values for the angular position of 60° and without, with a linear fit. b) Shows the mean without 60° compared to the simulation of the different baffle models with a different amount of rows. The fit parameters of all fits are displayed in Table 1.

angular position of 60° are smaller than with the 60° angle. The outlier is nearly twice as high as the second-highest transmittance, for the two most outer radial positions.

Measurement	a [%/cm]	b [%]	Transmitting radius [cm]
Simulation with 5 rows	0.04	-0.14	3.65
Simulation with 4.5 rows	0.92	-14.60	15.85
Simulation with 4 rows	1.78	-27.20	15.27
Simulation with 3.5 rows	3.26	-49.68	12.95
experimental mean w 60°	1.27	-15.15	11.92
experimental mean wo 60°	1.12	-14.53	12.95

Table 1: The table shows the fit parameters for the linear fit (Equation 6) of the data points in Figure 15. And the radius at which the baffle model starts to transmit light.

That 60° is such a big outlier follows from the clumping of the bristles (see Figure 13) at the 60° angle, leading to a higher transmittance, as mentioned in section 2.2 and shown in Figure 12. This outlier is ignored to more accurately represent the actual mean of the baffle. For errors on the simulated values it is assumed that the number of hits detected on the detector is Poisson distributed. To calculate the error on the light transmitted, Equation 3 is used.

The increase in transmittance of the baffle with higher radii is expected to be linear once the absorption is no longer a 100%. This follows from the area of a ring on the baffle with a given thickness rising linearly in radius, but the area that is blocked by the bristles is constant. This can be mathematically shown by calculating the radial dependency of the area A of the ring.

$$A = \int_{r_i}^{r_o} \int_0^{2\pi} r dr d\varphi = \pi(r_o^2 - r_i^2) \quad (4)$$

The inner and outer radius of the ring are r_i and r_o , if the inner and outer radius are replaced with the mean of the two radii \bar{r} and the difference between both Δr , the radial dependence can be calculated with:

$$A(\bar{r}) = 2\pi\bar{r}\Delta r \quad (5)$$

And this is linear in \bar{r} if the thickness of the ring Δr is constant. The area blocked by the bristles is a constant offset, meaning the baffle blocks light completely until some radius, this can be seen in Figure 15b. A linear function:

$$f(x) = ax + b \quad (6)$$

with the fit parameters a, b is fitted to the values in Figure 15 visibly larger than zero. The baffle model with the highest similarity to the experimental data will be chosen for further simulations. When comparing the different fits in Table 1 the biggest similarity comparing the fit parameters to the parameters in the experimental data has the baffle model with 4.5 rows. Looking at the relevant interval in the Figure 15 it becomes apparent that the best-fitting model would be the baffle model with 4 rows. Best fitting means here the smallest difference between model and experimental values and fit. This is also the best-fitting model if the 60° values are not ignored for the mean.

The difference between the simulation and experiment, results from the bristles of the experimental baffle clumping together and being overall less homogeneous. This

leads the baffle to be transmitting at a smaller radius than a simulated baffle with the same amount of bristles. For the coming simulation, the baffle needs to be the best approximation in actual transmittance, therefore the best-fitting model (the baffle model with 4 rows) is chosen.

2.4 Results

A working experimental setup to test the absorption of the baffle has been successfully built and used to map the angular and radial dependency of the absorption of the baffle. The result of the measurement has shown that the baffle blocks on average more than 91% (area weighted mean) of the light passing through it. This is highly dependent on the radial and angular position. The dependence on the angular value is more or less random and depends mainly on the bristles clumping together. The transmittance rises linearly with the radius, this is observed for all angular positions. The simulation of the experiment determined the baffle model with 4 rows of bristles to be the most similar to the experimentally used baffle. This model will be used for the coming simulations.

3 Simulation

In this chapter different simulations are presented, all simulations in this thesis are done with Zemax Opticstudio [36]. In the first chapter, a general simulation of the ice, recreating the optical medium of IceCube is created. The results of this simulation will be compared to a previous simulation in IceCube’s PPC [41].

In the second chapter, different simulations of a representation of the LOMlogger inside the borehole are simulated. The first three simulations are for a better understanding of the optical properties of the borehole itself. In the next simulation the impact of the baffle position inside the borehole on the detected light intensity on the detector is tested. In the same simulation the impact of the borehole radius on the effectiveness of the baffle is tested. The position where the baffle gets hit is tested in the last simulation for different distances to the source. This is done to better understand light path inside the borehole. We define ε as the detected hits divided by the total emitted rays of the source. This is done to be able to accurately compare the results of different simulations.

3.1 Scattering in ice simulation

This simulation aims to test the consistency of the simulation in Zemax compared to previous simulations with IceCube’s PPC (photon propagation code) [41]. Trying to recreate the photon rate of the LOMlogging project from only scattering inside ice of the previous simulation. The detected photon rate will be compared between both simulations.

The setup for the simulation consists of a cubic ice volume with a volume of $100 \times 100 \times 100 \text{ m}^3$, a source, and a detector, as seen in Figure 16. The source is a point source pointed orthogonal to the detector, similar to the setup of the LOMlogger, where the POCAM points orthogonal into the ice (see section 1.5.2). The detector is a plate with a radius of 16 cm, this is the best approximation of the LOM as a plate [22, 24]. The detector and source are placed 2 m apart and in the center of the cubic ice volume. The scattering inside the ice will be modeled with the Henyey-Greenstein scattering model ($g=0.95$ [2]), already implemented in Zemax. The Henyey-Greenstein scattering model is an approximation of Mie-scattering [27], and it is also used in the PPC. Contrary to PPC, absorption inside the ice is not modeled, due to Zemax having no good implementation for this. This would lead to slightly higher ε values, than PPC, therefore values of the PPC without absorption are also used.

The light scattered onto the detector is measured for 9 different logarithmically spaced effective scattering lengths between 6.32 m and 100 m and the effective scattering length of the cleanest ice in IceCube (84.14 m). The ε of the simulation in Zemax is roughly a factor of four larger than the ε simulated with the PPC. The reason for this large discrepancy between both simulations is unclear. The different detector shapes used in both simulations are the best explanations for this. The PPC simulation uses a model of the LOM as the detector and the simulation in Zemax only uses a plate. This leads to the assumption that the plate is not the best approximation to the LOM. In order to keep it simple the plate shape of the detector will still be used in further simulations. The coming simulations aim to compare their results with the expected photon rate from scattering in ice. This photon rate will be the photon rate of the simulation in Zemax with an effective scattering length of 84.14 m representing the cleanest ice in the IceCube

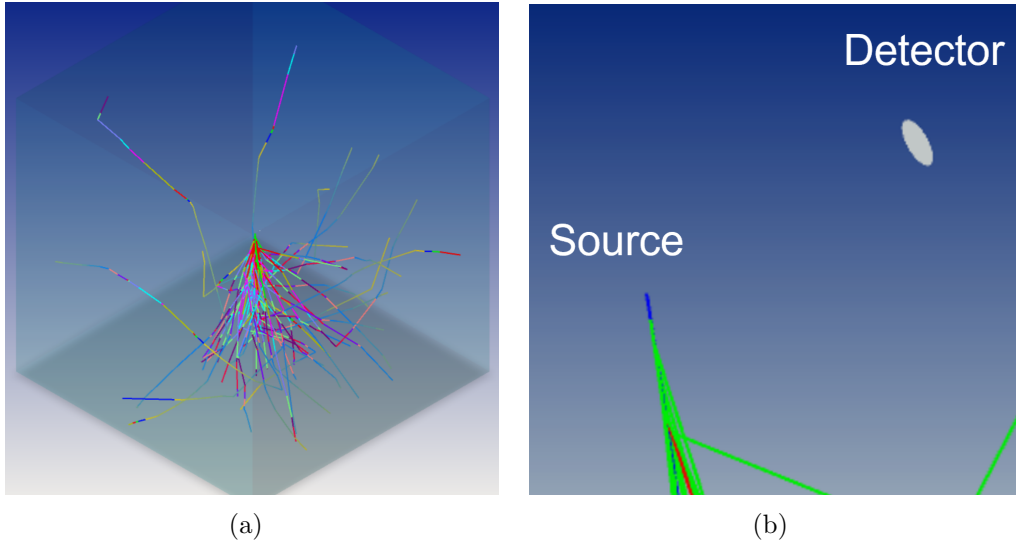


Figure 16: a) Shows the full cube of ice with the source and the detector and 20 simulated rays, the color of the rays change each time they scatter or reflect. The simulated effective scattering length of the ice depicted is 80 m. b) Shows the same simulation only zoomed in on the source and detector.

detector [2]. The rays detected per emitted ray is equal to $1.151 \cdot 10^{-5}$ Hits/Emitted rays. This photon rate is chosen, so the simulations can be compared within Zemax. The photon rate would lead to the smallest possible value from light scattering in the ice. If the light scattered inside the borehole is smaller than this value it can be considered noise and easily filtered out.

3.2 Simulation of the borehole

This simulation tries to mimic the properties of the borehole during deployment. With this, the main reason for light reaching the detector from inside the borehole will be investigated. In particular the impact of the reflection at the ice water surface and the scattering in the water of the borehole will be evaluated. Afterwards, the baffle will be introduced into the simulation and the optimal position of the baffle and the impact of a changing borehole diameter will be investigated.

3.2.1 Setup

The simulations assume the following simplifications of the borehole: The ice water surface is perfectly even, and the water and ice are completely homogeneous. The refractive index is assumed to be constant for water 1.3429 and for ice 1.3190 [42] at the simulated wavelength of 405 nm. These assumptions are reasonable for this simple model. The setup for the simulation consists of the following:

Ice The ice has cubic volume of 10^3 m^3 . There is no scattering implemented inside the ice.

Borehole The borehole is represented as a cylindrical water volume inside of the ice, with a radius of 26 cm. This is the expected radius of the borehole in the IceCube

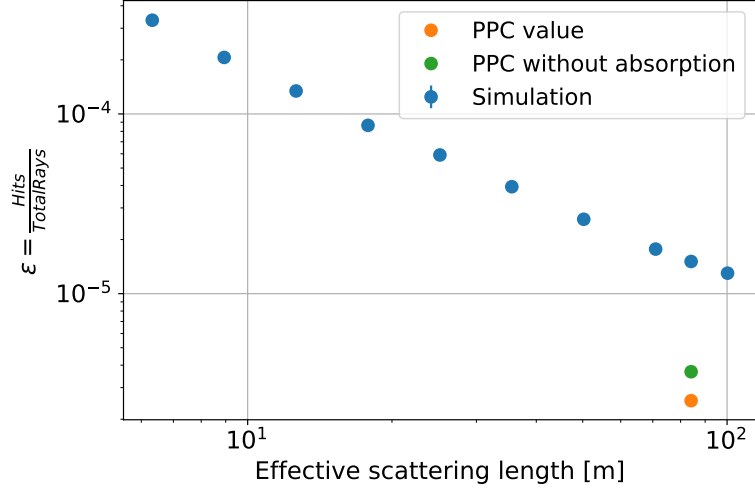


Figure 17: The plot shows the simulated rays detected per emitted ray plotted over the effective scattering length. Additional values which were simulated with the PPC with and without absorption are included in the plot. These values are the values for scattering in the cleanest ice, with an effective scattering length of 84.14 m.

Upgrade [43], the impact of the radius will be investigated in a coming simulation.

Source The source mimics the POCAM. The source has two angles one parallel to the detector plane and one orthogonal. The fanout angle parallel to the detector plane is 60° , equal to that of the POCAM. The angle orthogonal to the detector plane is 10° , which is larger than that of the POCAM but an approximation to the maximal swaying range of the POCAM [19]. The source is placed in the center of the water column and points orthogonal to the detector plane straight into the ice.

Detector The detector is the same as described in section 3.1. It is a plate with a radius of 16.2 cm and is placed inside the borehole 2 m away from the source, as seen in Figure 18a.

Baffle The baffle used here is the baffle that was chosen in section 2.3 to be the most accurate representation of the baffle used in the experiment. The position of the baffle will be determined in the given simulation.

This setup mimics the LOMlogger during deployment at a given depth in the borehole, the similarities can be seen in Figure 18.

3.2.2 Different angle between source and detector

In the following simulation, the angle of the source relative to the detector will be changed. The light reaching the detector will be measured. This is done to observe the impact of light reflecting at the ice-water surface on the total light reaching the detector.

For this simulation, the same setup is used as discussed in section 3.2.1 with the exception that the angular position of the source is changed as seen in Figure 19a and

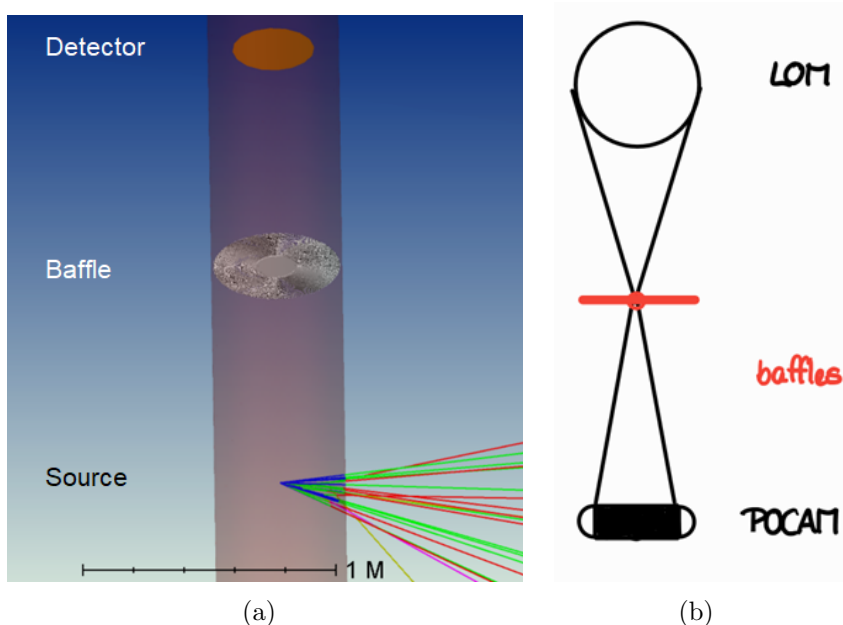


Figure 18: a) Shows an image of the borehole simulation. The detector represents the LOM and the source the POCAM. b) Shows a sketch of the LOMlogger setup [19].

without the baffle. The number of rays used for this simulation is $4 \cdot 10^9$ rays and which is the maximal rays Zemax can simulate at once. The angles for the simulation range from 55° to 90° , 0° meaning the standard position of the source pointing directly into the ice, and 90° meaning the source points directly onto the detector. The range goes only down to 55° because the detected light as seen in Figure 19b is already well below the threshold. This threshold is 10% of the value given by section 3.1, meaning the light scattered inside the borehole would be noise with a maximal amplitude of 10% of the light scattered in the cleanest ice. This threshold is not a fixed noise limit but only a guideline value. Additionally, smaller angles would need more simulated rays to achieve a decent signal and the simulation already reached the maximum of rays Zemax can handle.

The expectation of the reflected fraction can be obtained via the Fresnel equations. The fraction R we would expect to be reflected at the ice-water surface for the light hitting the surface vertically can be calculated with [44]:

$$R = \frac{n_1 - n_2}{n_1 + n_2} \quad (7)$$

We obtain with the refractive indexes of the water and ice used in the simulation $R = 0.9\%$. This value is very small this can also be seen in the simulation.

There is a big dip in intensity visible at an angle of 65° . This dip originates from the rays needing to reflect three instead of two times to reach the detector. With that the probability of the rays reaching the detector drops drastically. The light decreases with smaller angles due to the number of reflections increasing, and the light transmitted out of the borehole increases. That the detected light is already below the threshold at an angle of 60° shows that the reflection alone will have close to no impact at the acceptable range of the source used in the Upgrade being between 0° and 10° .

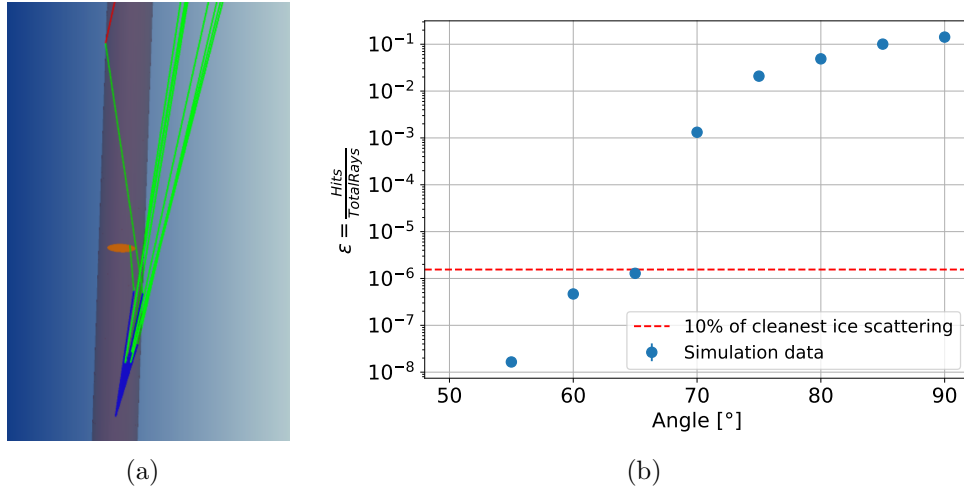


Figure 19: a) Shows the simulation setup for an angle of 80° , the reflection can be seen nicely, and the ray reflecting twice looks like total internal reflection. b) The plot shows the detected hits divided by the total emitted rays of the source plotted over the angle in degrees. The red dotted line marks 10% of the value given by section 3.1 as a threshold.

3.2.3 Scattering length

The impact of different scattering lengths inside the water column on the light reaching the detector will be analyzed, in the following simulation. This will be done with and without the baffle to see if the baffle performs worse at some scattering length or if it always blocks the same relative amount of light. The same simulation will be repeated with a plate of the same diameter as the baffle. This will then be compared to the baffle to see what is the best that the baffle could possibly achieve.

The setup is the same as described in section 3.2.1, with additional Henyey-Greenstein scattering implemented for the water column ($g=0.9$). This means reflection is also implemented. The baffle will be placed in the center between the source and the detector, this leads to a distance to the source of 1 m, for the simulation including the baffle. A simulation with a plate with the same diameter of the baffle at the same position of the baffle is also created. For all three setups, 13 data points with 13 different logarithmically spaced effective scattering lengths, reaching between 1 m and 100 m, are simulated. The results of the simulation are shown in Figure 20.

In Figure 20 the difference between with and without baffle seems to stay the same, so it seems that the baffle is performing consistently for the different scattering lengths. This is confirmed by the average amount of light transmitted. The average light transmitted through the baffle is $16.73 \pm 1.92 \%$, and for the plate it is $8.26 \pm 0.44 \%$, the error is the standard deviation on the mean. The transmittance of the baffle is twice as high as that of the plate, showing that using more than one baffle could be a valid idea.

The highest ϵ is at an effective scattering length of 3 m. The actual effective scattering length in the water of the borehole is not known. But an upper limit can be thought of, which is equal to the effective scattering length of the cleanest ice layer. The reason for this is that the scattering is driven by the amount of dust particles inside the water, and the least amount of dust particles that can be in the water is equal to the amount

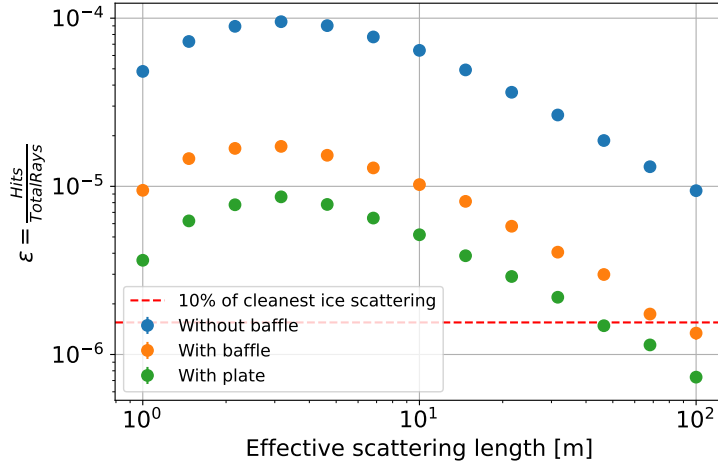


Figure 20: The plot shows the detected hits divided by the total emitted rays of the source plotted over the effective scattering length in meters, with and without the baffle and with a plate the same size as the baffle. The red dotted line marks the goal given by section 3.1.

of dust in the molten ice. So the cleanest water comes from the cleanest ice. This upper limit assumes that the drilling process does not introduce new impurities, this is why the actual scattering length is presumed to be much smaller. So for further simulations, we assume the worst case of 3 m effective scattering length.

The detected signal at the worst effective scattering length with the baffle is roughly a magnitude larger than the threshold. This leads to a signal-to-noise ratio (SNR) of 1.01 for the baffle which is clearly higher than that without the baffle of 0.17. The SNR is calculated by dividing the light scattered inside the cleanest ice with the light scattered inside the borehole at the scattering length of 3 m. The low SNR shows that the position of the baffle or the baffle is insufficient for blocking enough light.

A solution could be adding multiple baffles instead of one, the maximal light this would block is equal to the light blocked by an absorbing plate equal to the size of the baffle. The plate blocks more light than the baffle. But still over 8 % of the light pass the plate. Which corresponds to a SNR of 1.99, double the SNR of the baffle. This leads to the hypothesis that most of the light passes the baffle alongside the edge. Which could only be fixed by a larger baffle.

To test this hypothesis the simulated rays that hit the detector were drawn, these can be seen in Figure 21, for a smaller number of rays than in the actual simulation. While some rays pass through the baffle most pass around. These can be divided into two groups, one that reflects once at the height of the baffle and hits the detector directly. And one where it seems the rays reflect similarly to the total internal reflection in optical fibers multiple times at the same angle. Both these problems cannot be solved with a more absorbing baffle. But the first one could be potentially solved with a different baffle position, this will be tested in a coming simulation.

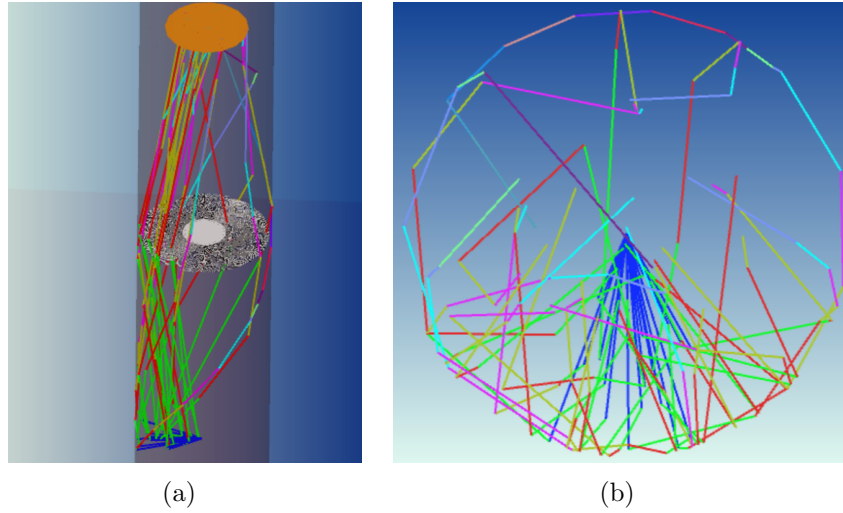


Figure 21: a) Shows the detected rays, the baffle, and the detector. b) The image shows the rays detected on the detector in the detector plane, without the baffle and detector.

3.2.4 Only backside of detector

In this chapter the impact of using only the backside of the detector is investigated. The light which reaches the backside of the detector needs to scatter at least one time more than it would need to reach the front side of the detector. This could lead to different results compared to section 3.2.3. The LOM as multiple PMTs facing in each direction. We could use for the stratigraphy measurement only the back facing PMTs. Showing this is a valid idea worth testing.

In a first step we need to recreate our comparison value for the scattering in the cleanest ice. This is done with the same simulation as in section 3.1, except only the backside of the detector can now detect rays. Resulting for the effective scattering length of 84.14 m to a ε of $3.4667 \cdot 10^{-6}$. This value is expectedly smaller than that in section 3.1. Because the rays need to scatter here also one more time to reach the detector.

The scattering simulation as in section 3.2.3 is redone with only the backside of the detector detecting. The results can be seen in Figure 22. The simulation with the baffle has relatively high errors because the number of detected photons is relatively low. And using more simulated rays would lead to the simulation taking more time than feasible. But the points are accurate enough to show the trend and give an approximation of the SNR. The highest ε is at the smallest effective scattering length of 1 m in contrary to the 3 m in Figure 20. This leads to the course of the data points to be shifted to the left. Resulting in better SNR for higher effective scattering lengths than around 2 m. If we compare the SNR for an effective scattering length of 3 m we obtain for the detector using both sides 0.17 and for using only the backside 0.42. The SNR for the backside only simulation is more than twice as high. The same is true for the simulation with the baffle. Here is the SNR for the simulation using the full detector 1.01 and for the only backside simulation 2.12. Using only the backside of the detector can be a good choice for higher scattering lengths. The problem with using only the backside of the detector is that the number of detected photons drops by over a magnitude. Therefore, using only the backside is only a good idea for high enough photon rates.

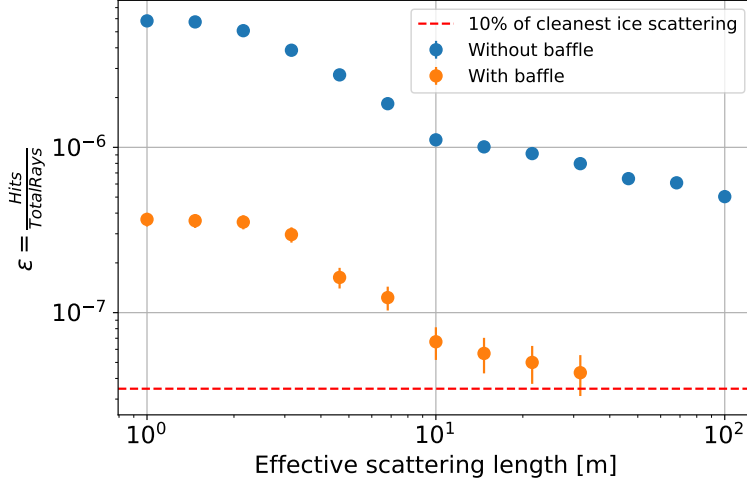


Figure 22: The plot shows the detected hits divided by the total emitted rays of the source plotted over the effective scattering length in meters, with and without the baffle. The dotted line marks 10% of the ε of $3.4667 \cdot 10^{-6}$ showing 10% of the scattering of the cleanest ice.

The good thing is here that we do not need to make a decision on whether we use only the backside of the detector or the full detector. Because we can do this later in the data analysis by choosing only the data of some PMTs. This shows that this is a valid idea during the data analysis which could increase the SNR by a lot without changing the setup of the LOMlogger. For the following simulations the full detector is used. As it results in higher photon counts and therefore better statistics. This is also the better choice as only the effectiveness of the baffle is investigated in the next simulations and that did not change by using only the backside of the detector.

3.2.5 Changing hole diameter and baffle position

This simulation intends to show the impact of the borehole diameter as well as the position of the baffle on the detected light. For this purpose, the setup of the simulations prior will be adopted. The diameter of the water column will be changed from 50 cm to 60 cm in 2 cm steps, this is the range the borehole is expected to be during deployment and a little above [43]. The baffle position will be changed relative to the source, from 0.25 m distance up to 1.75 m in 25 cm steps. The acquired data is plotted in Figure 23 as a 2D colormap.

From Figure 23 it becomes apparent that a larger borehole radius leads to more light passing the baffle. The reason for this is more space between the baffle and the ice, which leaves more space for the light to avoid the baffle.

A baffle position close to the detector or source is preferred. The reason for this behavior is that more light has to pass through the baffle, if the baffle is close to the detector, and with that, the baffle is more efficient. The problem with this position is that the baffle also blocks the detector from light scattered in ice or Cherenkov radiation rendering the detector module inefficient. The position close to the source, i.e. close to the POCAM, is more reasonable as this position was already proposed in an older design iteration

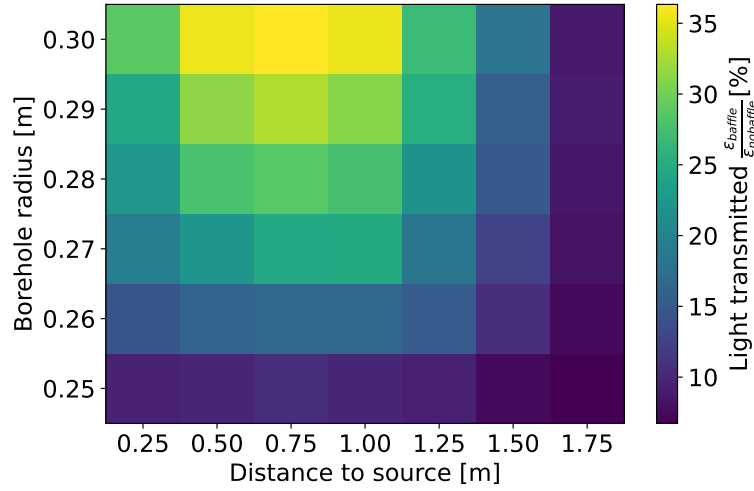


Figure 23: The plot shows the light transmitted through the baffle normalized with the values without the baffle in percent as color, for different baffle positions and Borehole radii.

[43] and would not impair the ability of the POCAM or LOM, the original design can be seen in Figure 24. The current design, placing the baffle in the center between LOM

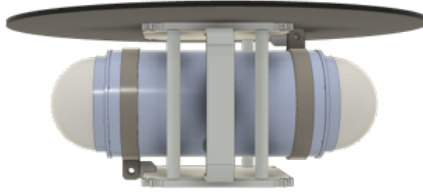


Figure 24: The image shows the proposed design of the baffle being attached on top of the pocam [43].

and POCAM is performing close to worst, so maybe the design needs to be overhauled. The real worse position is slightly asymmetrically biased to the source, at a distance of 0.75 m to the source. The reason for this bias will be investigated in the next simulation. The simulation showed that the light transmitted is extremely dependent on the borehole radius. Showing for larger boreholes a larger baffle would be best. It also showed that the current position of the baffle is not optimal and moving it to the POCAM could be an interesting idea or using more than one baffle.

3.2.6 Position where the baffle gets hit

The simulation aims to get a better understanding of the path the light takes, while propagating through the borehole and, with that an understanding of the asymmetry in the section 3.2.5. For this intent, the baffle and circular detector are removed from the setup and replaced with a square detector of 0.36 m^2 with 60×60 pixels, with each pixel having an area of 1 cm^2 . This detector will be positioned at different distances from the source. The position on which the detector is hit is now of interest, contrary to the

prior simulations. These images for the detector positions are shown in Figure 25.

The closer the detector is to the source the more focused the light is and more light is

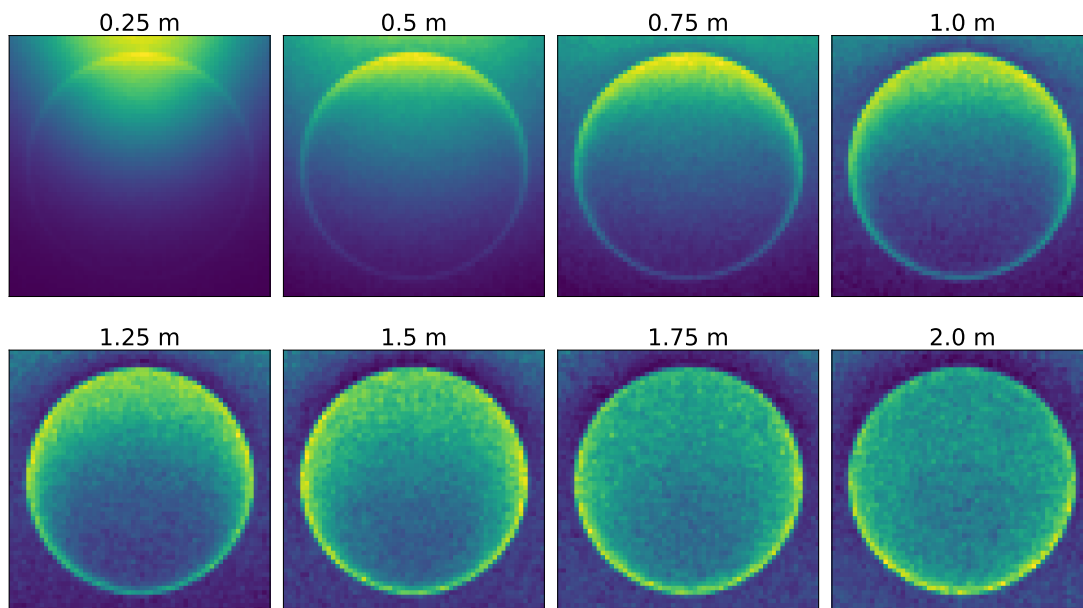


Figure 25: Eight images for eight detector positions are shown, as distance to source. Higher pixel brightness shows higher intensity. The images have a different scaling for the colors, this is not a problem because only the relative intensity for each image individually is of interest. The circle visible in the images is the cross-section of the borehole. The source points upwards, relative to these images.

at the edge of the borehole. Further away the light gets more evenly distributed inside the borehole. This is the reason for the asymmetry in section 3.2.5, closer to the source there is more light on the outer part of the borehole, and with that more light passes the baffle, leading to a higher transmittance, as seen in Figure 23. Closer to the detector the light is more evenly distributed and with that, the baffle blocks more light.

4 Conclusion

This thesis presented an analysis of the optical properties of the baffle considered for usage in the LOMlogger. The LOMlogger will be used in the Upgrade to measure the interaction lengths at different depths of the ice [33]. To obtain a less noisy measurement of the ice, baffles are used to block the light reflected and scattered inside the borehole. The effectiveness of the baffles has been investigated in this thesis. The baffle's transmittance is tested in an experiment, and this values is used for simulations of the baffle inside the borehole.

The experiment consists of a setup capable of measuring the transmittance of the baffle at different angular and radial position. The area dependent mean of the transmittance is roughly 9 %, meaning the baffle blocks over 91 % of the light passing through it. The transmittance is not constant for all positions. The transmittance rises linearly with the radius. The transmittance changes more or less randomly with the angle, due to bristles bunching together which lead to worse absorption.

The radial dependence of the baffle was compared with simulations of different baffle models. These models had different bristle densities and amount of rows. The baffle model with four rows and around 2000 bristles resembled the experimental baffle the closest and is used for the simulations of the borehole.

All simulations are done with Zemax Opticstudio [36]. The first simulation, simulates the scattering in a large ice medium. The results are compared to a simulation done with the PPC [41]. The results of the simulation with Zemax are a factor of 4 larger than the values of PPC, the discrepancy resulting most likely from the different detector shapes used in both simulations. The flux on the detector for scattering in the cleanest ice of the simulation in Zemax will be used as a threshold to compare to the values in the simulations of the borehole. The flux or the rays detected per emitted ray is equal to $1.151 \cdot 10^{-5}$ Hits/Emitted rays at an effective scattering length of 84.14 m.

The borehole in which the LOMlogger will be lowered in and the LOMlogger itself are reconstructed in the following simulations. The first simulation of this kind does not simulate the scattering inside the borehole or the baffle. It only simulates the scattering on the ice water surface. The impact on the intensity on the detector of different source angles is tested. The result showed that the detected light is already below the threshold at an angle of 60° shows that only reflection will have close to no impact at the acceptable range of the source used in the Upgrade being between 0° and 10° .

In the next simulation, the scattering of the light was also modeled. The scattering length inside the water of the borehole is unknown, therefore are different scattering lengths simulated and plotted. To ensure that the different scattering lengths have no impact on the relative amount of light which is blocked by the baffle, the setup is also simulated with the baffle. There is indeed close to no difference of the effectiveness of the baffle at different scattering lengths. The highest amount of light reaches the detector at an effective scattering length of 3 m. The same simulation is done with a plate instead of the baffle, to observe the maximal light multiple baffles would block. The average light transmitted of the different scattering lengths through the baffle is 16.73 ± 1.92 %, and for the plate it is 8.26 ± 0.44 %, the error is the standard deviation on the mean. The transmittance of the baffle is twice as high as that of the plate, showing it would be worth to use more than one baffle.

In an additional simulation, only the backside of the detector was used. As this could be a good idea to reduce the light reaching the detector from scattering in the borehole. Because the light would need to scatter at least one more time to reach the detector. This results into a shift to higher intensities for smaller effective scattering lengths. The shift results into better SNR for higher effective scattering lengths. The SNR is by roughly a factor of two better compared to using the full detector at effective scattering lengths larger than 2 m. The use of only the backside PMTs of the LOM could be a valid option, specially because this decision can be made after the measurement in the data analysis.

A following simulation investigated the best position of the baffle, and the impact of the borehole diameter. The result showed expectedly larger borehole radii having a higher transmittance than smaller. This is due to the light having more space to pass around the baffle at larger radii. The simulation also showed that the effectiveness of the baffle is highly dependent on the position of it relative to the source and the detector. The baffle being close to the detector or the source is better than the position directly between them. A prior design iteration close to the POCAM could be a better idea than placing it in between the POCAM and LOM.

The simulation of the effectiveness of the baffle at different positions relative to the POCAM has shown an asymmetry. For this the light distribution at the different baffle positions is investigated. This showed that the asymmetry originates from the light being more focused at the edge of the borehole close to the source, where the light just passes the baffle. The light gets more diffuse the further away from the source and with that the baffle is more effective.

The results of the simulation and experiment reveal that using only one baffle (SNR = 1.01) is not enough for a good signal-to-noise ratio. Therefore, the use of multiple or larger baffles would be a good solution to fix this. Another interesting idea would be to use two different baffle positions simultaneously. This would lead the rays needing to scattering at least twice to be able to hit the detector, and with that a potentially drastic reduction of light reaching the detector. A potential setup would be combining the baffle mounted to the POCAM and the baffle between POCAM and LOM.

Based on the results of this thesis, it is concluded that the baffle can be a good choice for the LOMlogger. The baffle with small adjustments to the setup can potentially lead to a high enough signal-to-noise ratio for the dust logging.

Acronyms

AMANDA Antarctic Muon and Neutrino Detector Array. 3

D-Egg Dual optical sensors in an Ellipsoid Glass for Gen2. 4

DOM digital Optical Module. 2

FWHM full width at half maximum. 4, 11

KM3NeT Kubikkilometer(km³)-Neutrino-Teleskop. 2

LOM long Optical Module. 5, 8, 9, 19, 22, 25, 27, 30

mDOM multi-PMT digital Optical Module. 4, 5, 8, 11

PBT Polybutylenterephthalat. 9

PMT Photomultiplier Tube. 4, 5, 8, 25, 26, 30, 32

POCAM precision optical calibration module. 4, 8, 9, 21, 22, 26, 27, 30

P-One Pacific Ocean Neutrino Experiment. 2

PPC photon propagation code. 19, 21, 29

SNR signal-to-noise ratio. 24, 25, 26, 30

A Test of the experimental results

The experimental setup used was not optimal, for that reason the representativeness of the results will be tested in the following. First we look at how the intensity of the flashers is distributed on the different radial positions of the baffle. Afterwards we look at which flasher caused the intensity.

The intensity distribution along the different radial positions of the photodiode is shown in Figure 26. Here are all flashers turned on, and the baffle is not simulated.

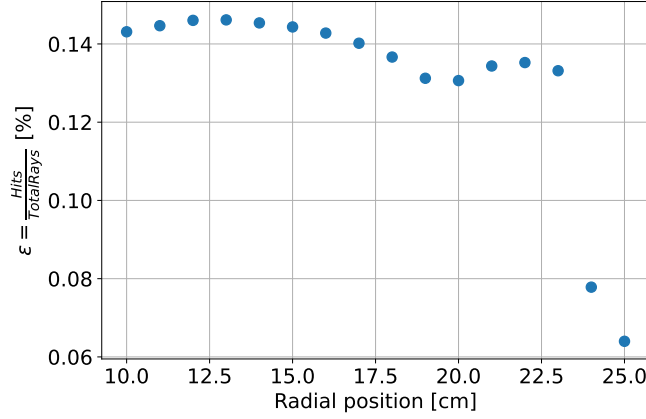


Figure 26: The plot shows the detected hits divided by the emitted rays in percent plotted over different radial positions of the photodiode.

The profile is nearly constant, but two arches are visible. These are the two intensity profiles of the two flashers over those radial positions, as seen in Figure 27.

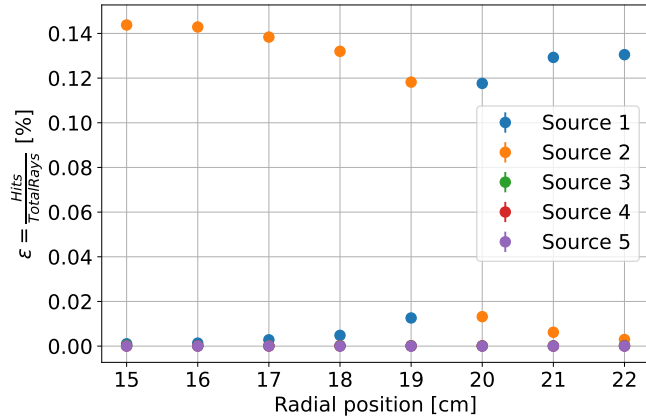


Figure 27: The plot shows the detected hits divided by the emitted rays in percent plotted over different radial positions of the photodiode. Each color represents the detected hits from one emitted of one source.

The relevant flashers are located at 13 cm and 26 cm. The wider peak is equal to the 15° opening angle of the flashers, this corresponds to a half width of $16 \text{ cm} \cdot \tan(15^\circ)$ equal to 4.3 cm at the height of the photodiode. The half width of the peak in Figure 26 is approximately 2 cm wider, the wider width follows from scattering of the rays while propagating through the water. The scattering length in this simulation was the scattering length of the highest intensity in Figure 20, approximately 3 m effective scattering length.

This means the light rays did not pass through the baffle directly above the photodiode

but on a slightly diffused path originating from one of the flasher positions. As seen in Figure 28 the actual positions of the light passing the baffle is slightly offset in respect to the photodiode.

$$a = \arctan\left(\frac{d}{H}\right) \quad \rightarrow \tan(a) \cdot h = r \quad (8)$$

Here is d the radial distance between the flasher and the photodiode, H the height difference between flasher and photodiode, h the height difference between baffle and photodiode and r the radius at which the ray passes through the baffle and a the angle as seen in Figure 28.

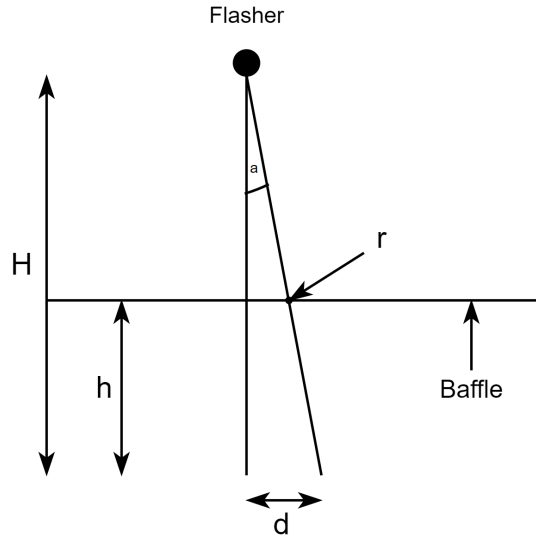


Figure 28: The plot shows the detected hits divided by the emitted rays in percent plotted over different radial positions of the photodiode. Each color represents the detected hits from one emitted of one source.

With this the actual positions of the light passing the baffle are shown in Table 2. The exact path is also not perfectly retraceable due to scattering in the water. This is shown as a rather large circles representing the position of the transmittance of the baffle in Figure 12.

Position of photodiode [cm]	Position through baffle [cm]
10	11.3
13	13
16	14.7
19	16.3
22	23.8

Table 2: The table shows the position of the photodiode and the with Equation 8 calculated position at which the light passed the baffle.

B Errors on the experimental results

In the following the errors of the experiment are displayed as well as the measured data. Each measurement consists of 30 measured photodiode intensities, these are averaged

and displayed in the following plots.

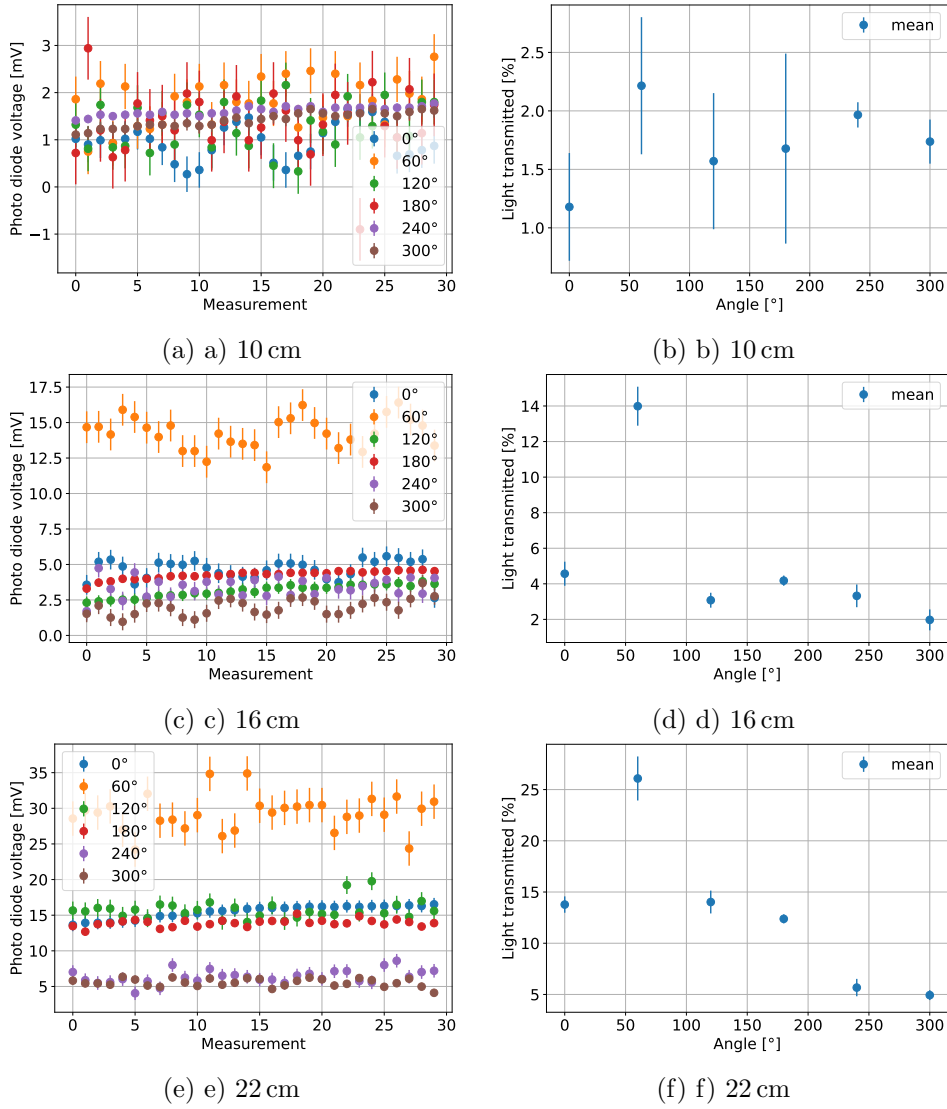


Figure 29: The left plots show the photodiode voltage in mV over the measurement number for all six angles. And the right plots show the average light transmittance over the 30 measurements, calculated with Equation 3. Plotted over the angle for each radius.

The mean of the different radii and angles is plotted in Figure 12, the mean values and their standard deviations are shown in the following table:

Radius [cm]	Angle [°]	Mean [%]	Standard deviation [%]
10	0	0.97	0.38
10	60	1.81	0.48
10	120	1.28	0.48
10	180	1.37	0.66
10	240	1.61	0.09
10	300	1.42	0.15
16	0	4.66	0.69
16	60	14.28	1.12
16	120	3.14	0.43
16	180	4.27	0.29
16	240	3.39	0.65
16	300	2.01	0.60
22	0	15.48	0.90
22	60	29.31	2.42
22	120	15.76	1.25
22	180	13.91	0.49
22	240	6.37	0.95
22	300	5.54	0.54

Table 3: Table with mean and standard deviation values of the light transmittance for each positional measurement of the experiment.

Bibliography

- [1] Thomas Gaisser and Francis Halzen. „IceCube“. In: *Annual Review of Nuclear and Particle Science* 64.1 (Oct. 19, 2014), pp. 101–123. ISSN: 0163-8998, 1545-4134. DOI: 10.1146/annurev-nucl-102313-025321. URL: <https://www.annualreviews.org/doi/10.1146/annurev-nucl-102313-025321> (visited on 07/08/2024).
- [2] Rasha Abbasi, Markus Ackermann, Jenni Adams, Nakul Aggarwal, et al. „In Situ Estimation of Ice Crystal Properties at the South Pole Using LED Calibration Data from the IceCube Neutrino Observatory“. In: *The Cryosphere* 18.1 (Jan. 4, 2024), pp. 75–102. ISSN: 1994-0424. DOI: 10.5194/tc-18-75-2024. URL: <https://tc.copernicus.org/articles/18/75/2024/> (visited on 05/06/2024).
- [3] Thomas K. Gaisser. „Neutrino Astronomy With IceCube at the South Pole“. In: *Marine Technology Society Journal* 48.5 (2014), pp. 35–39. ISSN: 0025-3324. DOI: doi:10.4031/MTSJ.48.5.5. URL: <https://www.ingentaconnect.com/content/mts/mts/2014/00000048/00000005/art00005>.
- [4] B. Pontecorvo. „Inverse Beta Processes and Nonconservation of Lepton Charge“. In: *Zh. Eksp. Teor. Fiz.* 34 (1957), p. 247.
- [5] Antonio Ereditato. *The State of the Art of Neutrino Physics, A Tutorial for Graduate Students and Young Researchers*. World Scientific, 2018. ISBN: 978-981-322-610-4. DOI: <https://doi.org/10.1142/10600>.
- [6] Claus Grupen. *Astroparticle Physics*. 2nd ed. Springer, 2020. ISBN: 978-3-030-27341-5. URL: <https://doi.org/10.1007/978-3-030-27339-2>.
- [7] Claus Grupen. *Astroparticle Physics*. Springer Berlin, 2005. ISBN: 978-3-540-25312-9.
- [8] Markus Ahlers, Klaus Helbing, and Carlos Pérez de los Heros. „Probing Particle Physics with IceCube“. In: *The European Physical Journal C* 78.11 (Nov. 13, 2018), p. 924. ISSN: 1434-6052. DOI: 10.1140/epjc/s10052-018-6369-9. URL: <https://doi.org/10.1140/epjc/s10052-018-6369-9> (visited on 07/16/2024).
- [9] Annarita Margiotta. „The KM3NeT Deep-Sea Neutrino Telescope“. In: *Nuclear Instruments and Methods in Physics Research Section A: Accelerators, Spectrometers, Detectors and Associated Equipment*. RICH2013 Proceedings of the Eighth International Workshop on Ring Imaging Cherenkov Detectors Shonan, Kanagawa, Japan, December 2-6, 2013 766 (Dec. 1, 2014), pp. 83–87. ISSN: 0168-9002. DOI: 10.1016/j.nima.2014.05.090. URL: <https://www.sciencedirect.com/science/article/pii/S0168900214006433> (visited on 07/22/2024).
- [10] Matteo Agostini, Michael Böhmer, Jeff Bosma, Kenneth Clark, et al. „The Pacific Ocean Neutrino Experiment“. In: *Nature Astronomy* 4.10 (Oct. 2020), pp. 913–915. ISSN: 2397-3366. DOI: 10.1038/s41550-020-1182-4. URL: <https://www.nature.com/articles/s41550-020-1182-4> (visited on 07/22/2024).
- [11] T. Benson, J. Cherwinka, M. Duvernois, A. Elcheikh, et al. „IceCube Enhanced Hot Water Drill Functional Description“. In: *Annals of Glaciology* 55.68 (Jan. 2014), pp. 105–114. ISSN: 0260-3055, 1727-5644. DOI: 10.3189/2014AoG68A032.

- URL: <https://www.cambridge.org/core/journals/annals-of-glaciology/article/icecube-enhanced-hot-water-drill-functional-description/F2A93B250A9FDB4E8A94101787BA3A68> (visited on 07/28/2024).
- [12] M. G. Aartsen, M. Ackermann, J. Adams, J. A. Aguilar, et al. *Neutrino astronomy with the next generation IceCube Neutrino Observatory*. en. arXiv:1911.02561 [astro-ph]. Nov. 2019. URL: <http://arxiv.org/abs/1911.02561> (visited on 07/07/2024).
- [13] Thomas Gaisser and Francis Halzen. „IceCube“. In: *Annual Review of Nuclear and Particle Science* 64. Volume 64, 2014 (2014), pp. 101–123. ISSN: 1545-4134. DOI: <https://doi.org/10.1146/annurev-nucl-102313-025321>. URL: <https://www.annualreviews.org/content/journals/10.1146/annurev-nucl-102313-025321>.
- [14] M. G. Aartsen, R. Abbasi, Y. Abdou, M. Ackermann, et al. „First Observation of PeV-Energy Neutrinos with IceCube“. In: *Phys. Rev. Lett.* 111 (2 July 2013), p. 021103. DOI: 10.1103/PhysRevLett.111.021103. URL: <https://link.aps.org/doi/10.1103/PhysRevLett.111.021103>.
- [15] R. Abbasi, M. Ackermann, J. Adams, J. A. Aguilar, et al. „The IceCube High-Energy Starting Event Sample: Description and Flux Characterization with 7.5 Years of Data“. In: *Physical Review D* 104.2 (July 8, 2021), p. 022002. ISSN: 2470-0010, 2470-0029. DOI: 10.1103/PhysRevD.104.022002. arXiv: 2011.03545 [astro-ph, physics:hep-ex, physics:hep-ph]. URL: <http://arxiv.org/abs/2011.03545> (visited on 07/22/2024).
- [16] *Observation of High-Energy Neutrinos from the Galactic Plane*. DOI: 10.1126/science.adc9818. URL: <https://www.science.org/doi/10.1126/science.adc9818> (visited on 07/16/2024).
- [17] ICECUBE COLLABORATION, Mark Aartsen, Markus Ackermann, Jenni Adams, et al. „Neutrino Emission from the Direction of the Blazar TXS 0506+056 Prior to the IceCube-170922A Alert“. In: *Science* 361.6398 (July 13, 2018), pp. 147–151. DOI: 10.1126/science.aat2890. URL: <https://www.science.org/doi/full/10.1126/science.aat2890> (visited on 07/22/2024).
- [18] Aya Ishihara. *The IceCube Upgrade – Design and Science Goals*. Aug. 25, 2019. DOI: 10.48550/arXiv.1908.09441. arXiv: 1908.09441 [astro-ph, physics:physics]. URL: <http://arxiv.org/abs/1908.09441> (visited on 07/08/2024). Pre-published.
- [19] Anna Eimer. personal correspondence. 2024.
- [20] Wing Yan Ma and for the IceCube collaboration. „Physics Potential of the IceCube Upgrade“. In: *Journal of Physics: Conference Series* 1468.1 (Feb. 2020), p. 012169. DOI: 10.1088/1742-6596/1468/1/012169. URL: <https://dx.doi.org/10.1088/1742-6596/1468/1/012169>.
- [21] Christian Fruck, Felix Henningsen, Christian Spannfellner, and IceCube Collaboration. „The POCAM as Self-Calibrating Light Source for the IceCube Upgrade“. In: *Proceedings of 36th International Cosmic Ray Conference — PoS(ICRC2019)*.

- 36th International Cosmic Ray Conference. Madison, WI, U.S.A.: Sissa Medialab, July 22, 2019, p. 908. DOI: 10.22323/1.358.0908. URL: <https://pos.sissa.it/358/908> (visited on 07/16/2024).
- [22] V. Basu and on behalf of the IceCube-Gen2 collaboration. „A Multi-PMT Optical Sensor for IceCube-Gen2“. In: *Journal of Instrumentation* 16.11 (Nov. 2021), p. C11009. ISSN: 1748-0221. DOI: 10.1088/1748-0221/16/11/C11009. URL: <https://dx.doi.org/10.1088/1748-0221/16/11/C11009> (visited on 07/12/2024).
- [23] Anna Nelles and IceCube-Gen2 collaboration. „Towards IceCube-Gen2: Plans for the in-Ice Radio Array“. In: *Proceedings of 9th International Workshop on Acoustic and Radio EeV Neutrino Detection Activities — PoS(ARENA2022)*. 9th International Workshop on Acoustic and Radio EeV Neutrino Detection Activities. Santiago de Compostela, Spain: Sissa Medialab, May 23, 2023, p. 057. DOI: 10.22323/1.424.0057. URL: <https://pos.sissa.it/424/057> (visited on 07/16/2024).
- [24] M.G. Aartsen, R. Abbasi, Y. Abdou, M. Ackermann, et al. „Measurement of South Pole ice transparency with the IceCube LED calibration system“. In: *Nuclear Instruments and Methods in Physics Research Section A: Accelerators, Spectrometers, Detectors and Associated Equipment* 711 (2013), pp. 73–89. ISSN: 0168-9002. DOI: <https://doi.org/10.1016/j.nima.2013.01.054>. URL: <https://www.sciencedirect.com/science/article/pii/S0168900213001460>.
- [25] P. Askebjør, S. W. Barwick, L. Bergström, A. Bouchta, et al. „Optical Properties of the South Pole Ice at Depths Between 0.8 and 1 Kilometer“. In: *Science* 267.5201 (Feb. 24, 1995), pp. 1147–1150. DOI: 10.1126/science.267.5201.1147. URL: <https://www.science.org/doi/abs/10.1126/science.267.5201.1147> (visited on 07/22/2024).
- [26] The IceCube Collaboration. „South Pole Glacial Climate Reconstruction from Multi-Borehole Laser Particulate Stratigraphy“. In: *Journal of Glaciology* 59.218 (Jan. 2013), pp. 1117–1128. ISSN: 0022-1430, 1727-5652. DOI: 10.3189/2013JoG13J068. URL: <https://www.cambridge.org/core/journals/journal-of-glaciology/article/south-pole-glacial-climate-reconstruction-from-multiborehole-laser-particulate-stratigraphy/61F8A53A3D396078677EB197234F970A> (visited on 06/13/2024).
- [27] J. Lundberg, P. Miocinovic, K. Woschnagg, T. Burgess, et al. *Light tracking through ice and water – Scattering and absorption in heterogeneous media with Photonics*. Aug. 29, 2007. DOI: 10.1016/j.nima.2007.07.143. arXiv: astro-ph/0702108. URL: <http://arxiv.org/abs/astro-ph/0702108> (visited on 05/28/2024).
- [28] M. Ackermann, J. Ahrens, X. Bai, M. Bartelt, et al. „Optical Properties of Deep Glacial Ice at the South Pole“. In: *Journal of Geophysical Research: Atmospheres* 111.D13 (2006). ISSN: 2156-2202. DOI: 10.1029/2005JD006687. URL: <https://onlinelibrary.wiley.com/doi/abs/10.1029/2005JD006687> (visited on 05/14/2024).

- [29] Kurt Woschnagg. „Optical Properties of South Pole Ice at Depths from 140 to 2300 Meters“. In: *26th International Cosmic Ray Conference (ICRC26), Volume 2* (1999), p. 200. URL: <https://adsabs.harvard.edu/full/1999ICRC...2..200W>.
- [30] Dmitry Chirkin and Martin Rongen. *An Improved Mapping of Ice Layer Undulations for the IceCube Neutrino Observatory*. July 26, 2023. arXiv: 2307.13951 [astro-ph]. URL: <http://arxiv.org/abs/2307.13951> (visited on 07/16/2024). Pre-published.
- [31] V. Basu and on behalf of the IceCube-Gen2 collaboration. „A multi-PMT optical sensor for IceCube-Gen2“. In: *Journal of Instrumentation* 16.11 (Nov. 2021), p. C11009. DOI: 10.1088/1748-0221/16/11/C11009. URL: <https://dx.doi.org/10.1088/1748-0221/16/11/C11009>.
- [32] Anna Eimer. *LOMlogging PDR: III. Optics design*. Feb. 2024. URL: <https://docs.google.com/presentation/d/1t7C6vHG36T1WZOSR4X6hDVI3Gt5CAVoBx2ab9skkP10/edit?pli=1#slide=id.p>.
- [33] Anna Eimer. *LOMlogging PDR: I. Overview*. Feb. 2024. URL: https://docs.google.com/presentation/d/1BKPKG1usbjU3wy_chGdYa0_EXAfzmWMv1T8fTzHKupM/edit#slide=id.g2686e0b081b_0_675.
- [34] Product site of the baffle, product number of baffle: 100178. URL: <https://bmtonline.de/en/ringbuersten-besatz-nach-aussen/> (visited on 07/06/2024).
- [35] Autodesk Fusion, CAD software. URL: <https://www.autodesk.de/products/fusion-360>.
- [36] Ansys Zemax Opticstudio, simulation software. URL: <https://www.ansys.com/de-de/products/optics/ansys-zemax-opticstudio>.
- [37] IceCube collaboration. *The LED calibration systems for the mDOM and D-Egg sensor modules of the IceCube Upgrade: Design, production, testing and use in module calibration*. Prepared for submission to JINST.
- [38] Datasheet of the RLT405-600MGE LED. URL: https://www.roithner-laser.com/datasheets/led_div/xrl-400-5o.pdf.
- [39] Datasheet of the S2281 Si photodiode from Hamamatsu. URL: https://www.hamamatsu.com/content/dam/hamamatsu-photonics/sites/documents/99_SALES_LIBRARY/ssd/s2281_series_kspd1044e.pdf.
- [40] Delia Tosi and Christopher Wendt. „Calibrating photon detection efficiency in IceCube“. In: *PoS TIPP2014* (2014), p. 157. DOI: 10.22323/1.213.0157. arXiv: 1502.03102 [physics.ins-det].
- [41] Dmitry A Chirkin. *IceCube/PPC: Version 1.0 (V1.0)*. Zenodo. 2023. DOI: 10.5281/zenodo.10410726.
- [42] M. N. Polyanskiy. *Refractive index of ice*. 2024. DOI: <https://doi.org/10.1038/s41597-023-02898-2>. URL: <https://refractiveindex.info/?shelf=3d&book=crystals&page=ice> (visited on 07/08/2024).

- [43] Martin Rongen. *LOMlogging PDR: V. Mechanical design*. Feb. 2024. URL: https://docs.google.com/presentation/d/1ztdQvmZIBB3jDY--B1LgrsXkMpJJ9_Ha2pRCLgZr9XQ/edit#slide=id.g268aa52b43e_0_0.
- [44] Wolfgang Demtröder. „Elektromagnetische Wellen in Materie“. In: *Experimentalphysik 2: Elektrizität und Optik*. Ed. by Wolfgang Demtröder. Berlin, Heidelberg: Springer, 2017, pp. 209–248. ISBN: 978-3-662-55790-7. DOI: 10.1007/978-3-662-55790-7_8. URL: https://doi.org/10.1007/978-3-662-55790-7_8 (visited on 07/29/2024).

Danksagung

First and foremost, I want to thank all IceCube group members at ECAP for seamlessly incorporating me into the group.

I am particularly grateful to Dr. Martin Rongen and Anna Eimer for helping me with all my questions. It was a lot of fun working with you!

Special thanks to Stephen Weybrecht for making the entire process of working on this thesis more enjoyable.

Lastly, I want to express my gratitude to my family for their unwavering support throughout my studies and making it possible for me to pursue this degree.

Eigenständigkeitserklärung

Hiermit versichere ich, Dean Eric Fleischmann (22956008), die vorgelegte Arbeit selbstständig und ohne unzulässige Hilfe Dritter sowie ohne die Hinzuziehung nicht offengelegter und insbesondere nicht zugelassener Hilfsmittel angefertigt zu haben. Die Arbeit hat in gleicher oder ähnlicher Form noch keiner anderen Prüfungsbehörde vorgelegen und wurde auch von keiner anderen Prüfungsbehörde bereits als Teil einer Prüfung angenommen.

Die Stellen der Arbeit, die anderen Quellen im Wortlaut oder dem Sinn nach entnommen wurden, sind durch Angaben der Herkunft kenntlich gemacht. Dies gilt auch für Zeichnungen, Skizzen, bildliche Darstellungen sowie für Quellen aus dem Internet.

Mir ist insbesondere bewusst, dass die Nutzung künstlicher Intelligenz verboten ist, sofern diese nicht ausdrücklich als Hilfsmittel von dem Prüfungsleiter bzw. der Prüfungsleiterin zugelassen wurde. Dies gilt insbesondere für Chatbots (insbesondere ChatGPT) bzw. allgemein solche Programme, die anstelle meiner Person die Aufgabenstellung der Prüfung bzw. Teile derselben bearbeiten könnten.

Ort, Datum

Unterschrift